A&A, 706, A330 (2026)
https://doi.org/10.1051/0004-6361/202557732

Astronomy & Astrophysics

A survey of molecular clouds in the Galactic center's outflow

Enrico M. Di Teodoro[1,2,⋆], Mark Heyer[3], Mark R. Krumholz[4], Lucia Armillotta[1,2,5], Felix J. Lockman[6], Andrea Afruni[1], Michael P. Busch[7], Naomi M. McClure-Griffiths[4], Karlie A. Noon[4], Nicolas Peschken[1], and Qingzheng Yu[1]

[1] Università di Firenze, Dipartimento di Fisica e Astronomia, via G. Sansone 1, 50019 Sesto Fiorentino, Firenze, Italy
[2] INAF – Osservatorio Astrofisico di Arcetri, Largo E. Fermi 5, 50125 Firenze, Italy
[3] Astronomy Department, University of Massachusetts, Amherst, MA 01003, USA
[4] Research School of Astronomy and Astrophysics – The Australian National University, Canberra, ACT 2611, Australia
[5] Department of Astrophysical Sciences, Princeton University, Princeton, NJ 08544, USA
[6] Green Bank Observatory, Green Bank, WV 24944, USA
[7] National Radio Astronomy Observatory, 520 Edgemont Road, Charlottesville, VA 22903, USA

Received 17 October 2025 / Accepted 17 December 2025

ABSTRACT

The nucleus of the Milky Way is known to drive a large-scale, multiphase galactic outflow, with gas phases ranging from the hot highly ionized component to the cold molecular one. In this work, we present the first systematic search for molecules in the Milky Way wind. We used the Atacama Pathfinder EXperiment (APEX) to observe the ^{12}CO(2→1) emission line in 19 fields centered on previously known high-velocity atomic hydrogen (HI) clouds associated with the outflow. Over 200 CO clumps are detected within 16 different HI clouds. These clumps have typical radii of 1–3 parsec, high velocity dispersions of 1–6 km s^{-1}, and molecular gas masses ranging from a few to several hundred $M_\odot$. Molecular clumps in the wind sit at the low-mass end of the mass–size relation of regular molecular clouds, but are far displaced from the mass (or size) – linewidth relation, being generally more turbulent and showing high internal pressures. Nearly 90% of the clumps are gravitationally unbound with virial parameters of $\alpha_{\rm vir} \gg 10$–100, indicating that these structures are either being disrupted or else confined by external pressure from the surrounding hot medium. While the observed properties of CO clumps do not seem to evolve clearly with latitude, we find that molecular gas is not detected in any of the 6 HI clouds with projected distances over 1 kpc from the Galactic center, suggesting the existence of a maximum timescale of ~3 Myr for the dissociation of molecular gas within the wind. Overall, current observations in the Galactic center support a scenario in which a hot wind entrains cold gas clouds from the disk, driving their progressive transformation from molecular to atomic and ultimately ionized gas through stripping, turbulence, and dissociation.

Key words. ISM: clouds – ISM: molecules – Galaxy: center – Galaxy: evolution

1. Introduction

Our Galaxy, the Milky Way (MW), hosts a large-scale, multiphase gas outflow in its nuclear regions (see review by Sarkar 2024). The γ-ray Fermi bubbles (Su et al. 2010) and the X-ray eROSITA bubbles (Predehl et al. 2020) are striking evidence of fast-moving outflowing gas containing both hot ($T > 10^6$ K) and nonthermal (particle energy $\gtrsim$ GeV) components, extending to over 10 kpc from the Galactic center (GC). Ultraviolet (UV) absorption studies have revealed the presence of high-velocity warm ionized gas ($T \sim 10^{4-5}$ K) across the volume of these bubbles (Fox et al. 2015; Bordoloi et al. 2017; Cashman et al. 2023). Closer to the Galactic plane, a population of high-velocity cool neutral gas ($T \sim 10^{3-4}$ K) clouds associated with the outflow were also detected thanks to observations of the atomic hydrogen (HI) emission line at 21 cm (McClure-Griffiths et al. 2013; Di Teodoro et al. 2018). Some of these clouds host cold molecular gas cores ($T \sim 10^{1-3}$ K), which have been detected either in carbon monoxide (CO) emission (Di Teodoro et al. 2020; Heyer et al. 2025) or in H_2 absorption (Cashman et al. 2021). These outflows could be powered by either recent activity from Sagittarius A* (e.g., Zubovas & Nayakshin 2012; Bland-Hawthorn et al. 2019) or the intense star formation in the inner Galaxy (e.g., Crocker et al. 2015; Sarkar et al. 2015), both in the Central Molecular Zone (CMZ, e.g., Barnes et al. 2017; Henshaw et al. 2023) and in the nuclear star cluster (e.g., Schödel et al. 2014; Nogueras-Lara et al. 2020).

Similar multiphase outflows, driven by either intense star formation or active galactic nucleus (AGN) activity, are observed in many galaxies across the Universe (e.g., Veilleux et al. 2020). These phenomena play a crucial role in the evolution of galaxies. By circulating and removing metal-enriched gas, they regulate star formation and stellar mass assembly, as well as the distribution of metals within and around galaxies (e.g., Naab & Ostriker 2017). Over the years, numerous theoretical studies have employed high-resolution (magneto)hydrodynamical (MHD) simulations to investigate the detailed physics underlying the launching and the evolution of galactic winds (see review by Thompson & Heckman 2024). A general consensus of these studies is that, while the hot gas phase carries most of the energy, a significant fraction of the wind's mass resides in the cool and cold phases (e.g., Kim et al. 2020; Schneider et al. 2020; Wibking & Krumholz 2023; Vijayan et al. 2024, 2025), especially at the wind base. It is therefore particularly important to understand the role of cooler phases in galactic winds.

⋆ Corresponding author: enrico.diteodoro@unifi.it

The origin and fate of cool and cold clouds within a hot wind pose significant physical challenges. Clouds lifted from the disk and entrained within the hot wind must be accelerated to high velocities through one or more mechanisms, including gain of momentum from the hot gas (e.g., Schneider et al. 2020; Fielding & Bryan 2022), radiation pressure (e.g., Thompson et al. 2015; Zhang et al. 2018) and cosmic ray pressure (e.g., Peschken et al. 2023; Rathjen et al. 2023; Armillotta et al. 2024). However, the interaction between gas phases is typically destructive, and cold clouds are expected to be shredded and disrupted on short timescales (e.g., Scannapieco & Brüggen 2015; Schneider & Robertson 2017). Radiative cooling of the hot fast-moving gas, induced by turbulent mixing with a seed cloud, has been invoked to explain the cool gas survival (e.g., Gronke & Oh 2020; Banda-Barragán et al. 2021; Kanjilal et al. 2021). In this case, the cloud gains mass while also acquiring momentum from the faster hot gas. Other physical mechanisms that may extend cloud lifetimes include magnetic fields (e.g., Sparre et al. 2020; Grønnow et al. 2022), and, in some cases, thermal conduction (e.g., Brüggen & Scannapieco 2016; Armillotta et al. 2017). An alternative scenario proposes that cold gas can be formed out of the hot phase through thermal instabilities, once the wind has cooled enough by adiabatic expansion at large distances (e.g., Thompson et al. 2016; Richings & Faucher-Giguère 2018). Despite all these possible scenarios, it remains uncertain how effectively these processes operate under realistic conditions. High-resolution observations of cool gas in galactic winds are therefore fundamental to constrain these theoretical models of cloud acceleration and survival.

The nucleus of the MW is one of the few places in the Universe where we can observe individual cool clouds in an outflow and investigate their resolved structure, physical state, and kinematics on (sub)-parsec scales. A pioneering study by McClure-Griffiths et al. (2013) first identified a population of 86 high-velocity HI clouds in the inner Galaxy ($|\ell| < 5°, |b| < 5°$), observed with the Australia Telescope Compact Array (ATCA), and proposed that they may represent the cool atomic counterpart of the nuclear outflow. Follow-up deep surveys with the Green Bank Telescope (GBT) supported this interpretation, expanding the known distribution of HI clouds to ±15° (≃2 kpc) in both Galactic longitude and latitude (Di Teodoro et al. 2018). Recent data show that this population may extend even farther, reaching $b \sim 30°$ (Bordoloi et al. 2025). Identified HI clouds show an anomalous local standard of rest (LSR) velocity, i.e., their kinematics are not compatible with the rotation of the Galactic disk but rather with a biconical wind accelerating from the GC and reaching velocities of ∼300–350 km s^{-1} (Lockman et al. 2020). These data provided a first direct estimate of the acceleration and velocity of the MW's cool wind, and gave some important clues on other key parameters of the outflow, including its geometry, cool mass loading rate, luminosity, and lifetime.

Targeted follow-up observations with the Atacama Pathfinder EXperiment (APEX) of the ^{12}CO(2→1) emission line in two outflowing HI clouds (MW-C1 and MW-C2) revealed the presence of dense molecular clumps (Di Teodoro et al. 2020). More recently, ^{12}CO(1→0) emission from a third cloud (MW-C21), detected with the Large Millimeter Telescope (LMT), further expanded the inventory of known molecular clouds associated with the nuclear wind (Heyer et al. 2025). These pilot CO observations suggest that outflowing HI clouds may carry substantial amounts of molecular matter, up to 60%–80% of their total mass (Di Teodoro et al. 2020). They also provide some important insights into the physical state of the molecular clouds: they appear to be too molecule-rich to be in chemical equilibrium (Noon et al. 2023), dominated by compressive turbulence (Gerrard et al. 2024), and gravitationally unbound (Heyer et al. 2025). Overall, the evidence gathered so far, though based on only three molecular clouds, points toward a scenario in which molecular gas is swept up from the Galactic disk and entrained into the hot wind, rather than reformed in situ. In this picture, molecular gas is expected to gradually dissociate under the influence of the Galactic extreme UV radiation field (Vijayan & Krumholz 2024), and the clouds should also be shredded as they are accelerated away from the Galaxy. Additional support for a disk origin comes from observations of molecular gas at lower latitudes ($|b| \lesssim 3°$), likely entrained by the nuclear wind. In particular, CO emission has been detected in molecular structures in correspondence of the X-ray Galactic chimneys (Ponti et al. 2019, 2021), up to 100 pc from the GC (Veena et al. 2023), and, on much larger scales, at the disk-halo interface near the edge of the MW's inner HI cavity (Lockman 1984; Lockman & McClure-Griffiths 2016), at Galactocentric radii of $R \simeq 3$ kpc (Su et al. 2022). However, low-latitude ($|b| < 1°$) features are hard to attribute uniquely to the wind, as anomalous velocity structures can also be produced by noncircular streaming motions and shocks along the Galactic bar (e.g., Sormani et al. 2018).

Despite these important advances, a comprehensive characterization of the physical state of the cold gas entrained in the wind, its interaction with other gas phases, and the evolution and fate of these clouds remains elusive. One of the main limitations so far has been the very small number of molecular clouds observed. Our current understanding relies on only three CO detections, which precludes any statistical analysis. This work is a first step toward addressing this issue. Here we present the results of the first systematic exploration of the molecular gas content in the MW's nuclear wind. We expand the sample of clouds observed in ^{12}CO(2→1) with APEX, adding 17 new objects to the 2 clouds presented in Di Teodoro et al. (2020). Their physical and kinematic properties are investigated and compared with regular molecular clouds in the disk.

The remainder of this article is structured as follows. Section 2 presents our new observations of molecular gas in the GC outflow. In Sections 3 and 4, we describe in detail the techniques used for the analysis of the data and to derive the physical properties of the outflowing gas. We present our results on the molecular clump properties, scaling relations, and evolution in Section 5, discussing their implications in Section 6. Finally, we summarize and conclude in Section 7. Throughout this paper, we assume a distance to the GC of $D = 8.2$ kpc (GRAVITY Collaboration 2019), for which 25 arcsec correspond to about 1 pc.

2. Data

2.1. Cloud sample

To date, over 200 outflowing HI clouds have been detected in the inner 15 degrees of our Galaxy, including the 86 clouds published in McClure-Griffiths et al. (2013) and the 106 clouds cataloged in Di Teodoro et al. (2018). Figure 1 shows a map of these high-velocity clouds. The grayscale map represents the HI emission at the tangent points from the Galactic All Sky Survey (GASS, McClure-Griffiths et al. 2009), roughly tracing the gaseous disk in the inner region of the MW (Lockman & McClure-Griffiths 2016). The bluescale color map shows instead the HI column densities of outflowing gas clouds from our GBT survey of the GC, including both data from

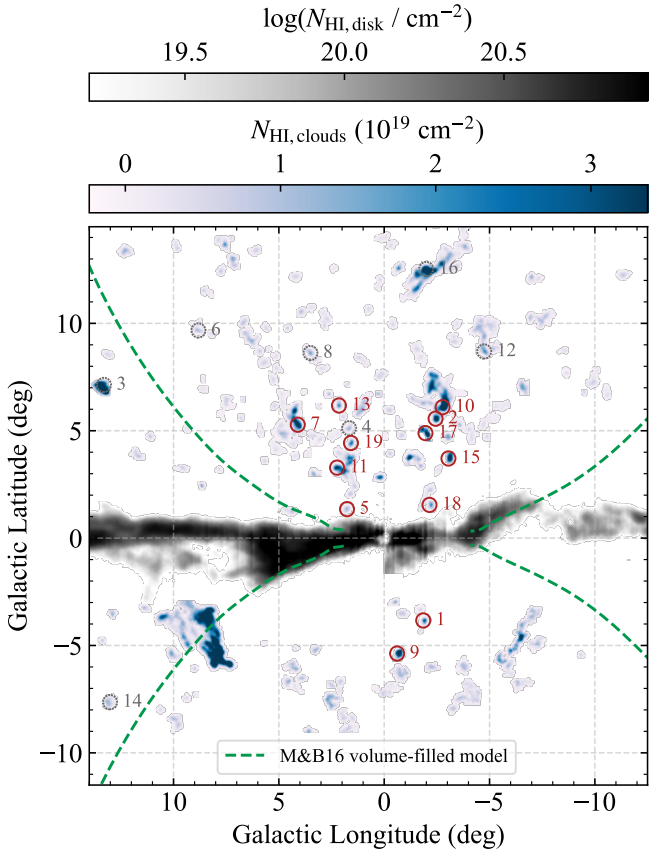

Fig. 1. Sample of high-velocity clouds studied in this work. The grayscale map represents the MW disk (Lockman & McClure-Griffiths 2016) and the blue color-scale map the outflowing HI high-velocity clouds (Di Teodoro et al. 2018). Red circles mark the clouds followed-up in the ^{12}CO(2→1) and ^{12}CO(4→3) lines with APEX and analyzed in this work, numbered as in Table 1. Dotted gray circles denote clouds not detected in CO emission.

Di Teodoro et al. (2018) and new data from more recent observations (Yu et al., in prep., Lockman et al., in prep.). As a reference, we also show the volume-filled model for the Fermi bubbles by Miller & Bregman (2016) as dashed green lines, representing the alleged boundaries of the bubbles. All these clouds have anomalous kinematics and are not in Galactic rotation. Most of them are very compact and have relatively low column densities (up to a few 10^{19} cm^{-2}), with the exception of a few larger and denser structures, such as the well-known "Shane feature" at $(l, b) \simeq (8°, -5°)$ (e.g., Burton & Liszt 1978).

In this work, we investigate the molecular gas component in a subsample of 19 outflowing HI clouds (including MW-C1 and MW-C2 from Di Teodoro et al. 2020), selected from a new updated catalog that combines the catalogs published in McClure-Griffiths et al. (2013) and Di Teodoro et al. (2018) with new detections found in our latest GBT HI observations. The clouds targeted are shown with red or gray circles in Figure 1 and listed in Table 1. This sample was chosen to cover a wide range in HI column densities and in Galactic longitude and latitude, with the idea of investigating both the relation between HI and molecular gas and the evolution of the cold gas as a function of distance from the GC. Out of the 19 clouds, three targets lie below the Galactic plane and sixteen above it. This north–south asymmetry mirrors that of the parent HI population and arises primarily from observational biases in our HI surveys (e.g., reduced GBT sensitivity and coverage at $b < 0°$) rather than from any intrinsic asymmetry in the wind (see Di Teodoro et al. 2018). Peak HI column densities of the APEX targets measured from the GBT data range between 5×10^{18} cm^{-2} and 8×10^{19} cm^{-2}. We emphasize that the GBT has a relatively low spatial resolution (570″) and that the measured column densities may be several times lower than the real ones because of beam dilution (see also Noon et al. 2023). For an assumed distance from the GC of 8.2 kpc, these clouds have HI masses between a few tens and a few thousand solar masses. The LSR velocities of the targets span from –260 km s^{-1} to +370 km s^{-1}, while typical HI line widths are in the range of 5–30 km s^{-1} (full width at half maximum, FWHM).

Table 1. Observational properties of the cloud sample observed with APEX.

Name	ℓ (°)	b (°)	V_{LSR} (km s^{-1})	OTF	σ_{rms} (mK)
MW-C1	−1.85	−3.83	+163	15′ × 15′	49
MW-C2	−2.44	+5.56	+265	15′ × 15′	34
MW-C3†	+13.30	+7.13	−100	15′ × 15′	65
MW-C4†	+1.66	+5.11	−262	10′ × 10′	80
MW-C5	+1.77	+1.35	−178	15′ × 15′	56
MW-C6†	+8.82	+9.67	+200	10′ × 10′	43
MW-C7‡	+4.10	+5.28	+205	10′ × 10′	51
MW-C8†	+3.50	+8.62	+365	10′ × 10′	55
MW-C9‡	−0.61	−5.37	−175	15′ × 15′	53
MW-C10‡	−2.77	+6.10	−165	15′ × 15′	55
MW-C11‡	+2.24	+3.28	−203	15′ × 15′	55
MW-C12†	−4.75	+8.69	−188	10′ × 10′	51
MW-C13	+2.15	+6.18	−217	15′ × 15′	60
MW-C14†	+13.01	−7.64	−182	15′ × 15′	50
MW-C15	−3.05	+3.71	+168	15′ × 15′	65
MW-C16†	−1.99	+12.53	−136	15′ × 15′	70
MW-C17	−1.96	+4.89	+230	15′ × 15′	57
MW-C18	−2.15	+1.55	−258	15′ × 15′	57
MW-C19	+1.58	+4.43	−226	15′ × 15′	59

Notes. † Not detected. ‡ Multi-velocity detections. Column 1 lists our assumed name, columns 2–4 give the Galactic coordinates and central velocity of the target, column 5 is the size of the on-the-fly map, and column 6 is the rms noise of the datacubes at 230 GHz in a 0.5 km s^{-1} channel.

2.2. Observations and data reduction

Millimeter and submillimeter data presented in this work were collected with the Atacama Pathfinder EXperiment (APEX) telescope under European Southern Observatory (ESO) dedicated time during observing periods P104 and P106 (Proposal IDs: 0104.B-0106A, 0106.B-0034A and 0106.C-0031A, Principal Investigator: Di Teodoro). Observations with the 12 m APEX antenna were spread across several ESO sessions, from November 2019 to April 2022. The weather conditions varied across the different observing sessions, with a precipitable water vapor (PWV) that ranged approximately between 0.5 mm and 3.5 mm.

Observations of MW-C1 and MW-C2 for the P104 period were carried out with the PI230 receiver tuned to map the ^{12}CO(2→1) emission line at 230.538 GHz. These data have been described and analyzed in Di Teodoro et al. (2020). For the P106 period, we targeted 17 additional clouds in the ^{12}CO(2→1) line with the new nFLASH230 receiver, which

replaced PI230 in 2020. Exploiting the possibility of using in parallel the nFLASH460 receiver, we also tried to detect the ^{12}CO(4→3) emission line at 461.041 GHz at the same time. The two spectrometer processors unit (FFTS) backends provide a bandwidth of 8 GHz for nFLASH230 and 4 GHz for nFLASH460, with a spectral resolution of 61 kHz, corresponding to roughly 0.08 km s^{-1} at 230 GHz and to 0.04 km s^{-1} at 460 GHz. The FWHM beam sizes are θ_{230} = 28.6″ and θ_{460} = 14.3″ at 230 GHz and at 460 GHz, respectively. These values correspond to linear resolutions of 1.1 pc and 0.6 pc at the distance of the GC. Average main beam efficiencies during the period of observations were $\eta_{\rm mb} = 0.80 \pm 0.06$ for nFLASH230 and $\eta_{\rm mb} = 0.60 \pm 0.05$ for nFLASH460[1]. Targets were observed in position-switching, on-the-fly (OTF) mapping mode, with sub-map sizes of 5′ × 5′, sampling every 9″, and using a dumping time of 1 second. For each target, either four or nine contiguous 5′ × 5′ submaps were covered, in order to reach a final field size of either 15′ × 15′ or 10′ × 10′. The coordinate centers of each map were chosen to align with the peak of the column density of HI derived from the GBT data. Integration times for each target were roughly 20 hours for the 15′ × 15′ maps and 10 hours for the 10′ × 10′. Map centers and sizes for all clouds in our sample are listed in Table 1.

The data reduction was performed using the Continuum and Line Analysis Single-dish Software (CLASS, Gildas Team 2013) and following standard data reduction steps. The data provided by APEX are spectra calibrated on the antenna temperature scale, T_A^*, which were converted to main beam brightness temperature through the measured main beam efficiency, i.e., $T_{\rm mb} = T_A^*/\eta_{\rm mb}$. A first-order baseline was then subtracted from each calibrated spectrum. During the process, we masked velocity channels where we expected to see emission based on the HI data, both from the high-velocity clouds and from the local interstellar medium at near-zero LSR velocity. Finally, after smoothing and resampling the spectra to a channel width of 0.5 km s^{-1} in the spectral range -400 km s^{-1} $\leq V_{\rm LSR} \leq$ +400 km s^{-1}, we gridded them into datacubes with a pixel size of 9″ at 230 GHz and of 5″ at 460 GHz, approximately one third of the expected main beam sizes. The root mean square (rms) noise $\sigma_{\rm rms}$ in our final datacubes at 230 GHz ranges between 34 and 80 mK for a 0.5 km s^{-1} channel (see Table 1), while at 460 GHz the rms noise varies between 200 mK and 500 mK. As was expected, none of the targets were detected in the ^{12}CO(4→3) emission line; thus, in the rest of this work we only focus on the analysis of the ^{12}CO(2→1) line data.

Finally, we also report on a failed attempt to detect the HCN(2→1) emission line at 177.239 GHz and the HCO$^+$(2→1) emission line at 178.376 GHz in the two densest CO clumps observed in MW-C1 (see Di Teodoro et al. 2020). HCN and HCO$^+$ lines typically trace denser molecular gas than ^{12}CO(2→1), with volume densities up to $n \simeq 10^4$ cm^{-3}. We used single pointing observations with the SEPIA180 receiver on APEX, integrated for about 3 hours for each clump, and reached rms noises in the reduced spectra of 7–10 mK for a 0.5 km s^{-1} channel width. Neither the HCN nor the HCO$^+$ species were detected in these two outflowing molecular clumps.

3. Cloud identification and characterization

For the analysis of the ^{12}CO(2→1) datacubes for our 19 targets, two main codes were exploited: ^{3D}BAROLO (3DB, hereinafter, Di Teodoro & Fraternali 2015) and PYCPROPS (Rosolowsky et al. 2021). The former is a code for galaxy kinematics, but it also features several useful functions to analyze emission line datacubes. In particular, 3DB was used to build masks that identify regions of genuine line emission and to derive moment maps from the datacubes. PYCPROPS is an improved, PYTHON implementation of the CPROPS algorithm (Rosolowsky & Leroy 2006) that was developed to study the properties of resolved molecular clouds in the PHANGS-ALMA galaxy survey (Leroy et al. 2021). This code can be used to assign voxels with emission to different sources and to calculate physical quantities, such as cloud position and size, integrated flux, luminosity, and molecular gas mass.

3.1. Emission line detection, masking, and moment maps

Regions of line emission in the datacubes were identified through the 3D source finder implemented in 3DB. In short, this algorithm identifies regions of contiguous voxels that lie above some primary flux threshold and then grows them adding more voxels at their edges down to a lower secondary threshold. Detections are then merged together based on criteria of proximity in both the spatial and spectral domains and finally they can be rejected/accepted depending on their size and/or spectral extent.

This approach relies on the noise level being constant throughout the datacube. Because each of our final datacubes is made up of several OTF sub-maps acquired during various observational runs and under different weather conditions, the noise level generally is not constant, but it can vary spatially from sub-map to sub-map. To overcome this issue, we ran the source finder on signal-to-noise (S/N) cubes rather than on the original data. To create the S/N cubes, we first derived noise maps $\sigma(x, y)$ for each target by calculating the noise level for each spectrum in each spatial pixel. The noise level was assumed to be the standard deviation of the data, computed via robust statistics, i.e., $\sigma(x, y) = 1.4826\,{\rm MADFM}(s(x, y))$, where MADFM is the median absolute deviation from the median of the spectrum $s(x, y)$ at the spatial position (x, y) and the factor 1.4826 converts between MADFM and standard deviation for normally distributed data. Finally, each channel map of the original cubes was divided by the noise maps to obtain the S/N cubes.

Source finding was performed on the resulting S/N cubes in the full LSR spectral range ±400 km s^{-1}, using a primary threshold of 3.5 and a secondary threshold of 2. We required reliable detections to cover at least the size of the beam and to extend over 1 km s^{-1} (= 2 channels). The source finder typically detects CO emission from local molecular gas in the solar neighborhood at $V_{\rm LSR} \sim 0$ km s^{-1} plus CO emission from high-velocity gas clouds. Line emission from local gas is detected in all observed fields but MW-C6. Because we are interested in studying only high-velocity clouds that may be associated with the GC outflow, we discarded all detections with a velocity that deviates less than 50 km s^{-1} from the expected Galactic rotation. High-velocity molecular gas is detected in nine of the 19 observed fields. Datacubes with no clear detections were smoothed to a channel width of 1 km s^{-1} and 2 km s^{-1} to reduce the noise level and the source finding process was repeated. This allows us to detect faint emission in three additional fields. All cubes were also carefully inspected to make sure that the source finder did not miss any faint but convincing emission.

In summary, high-velocity ^{12}CO(2→1) emission is detected in 12 out of 19 targets. Detected clouds are highlighted as full red circles in Figure 1, while non-detections are shown as dotted gray circles and indicated with a dagger in Table 1. MW-C12

[1] https://www.apex-telescope.org/telescope/efficiency/

and MW-C16 may have some very marginal signal at a $1.5\sigma_{\rm rms}$ level, but being so weak we decided not to include them in the list of detections. All CO sources have velocities consistent with the high-velocity HI cloud that was targeted. In four fields (MW-C7, MW-C9, MW-C10, MW-C11), we also detect a secondary component at a different velocity with respect to the targeted HI cloud: all these detections can be easily associated with additional high-velocity outflowing HI clouds that coincidentally falls into the observed field of our CO data. These sources will be labeled with a _2 throughout the paper (e.g., MW-C7_2). Taking also these secondary sources into account, we detect CO emission associated with a total of 16 HI clouds in the GC outflow.

For each target, we created a 3D mask $\mathcal{M}(x, y, v)$ identifying the voxels belonging to a detection. These masks were used during the analysis with PYCPROPS and to derive moment maps for all detected CO sources through 3DB. Figure 2 illustrates the APEX CO data for two clouds in our sample: MW-C10 (upper panels), a prototype of a cloud with abundant CO emission at high S/N, and MW-C13 (lower panels), a typical cloud with scarce and low S/N CO emission. For each cloud, we show a large-scale HI column density map (top left) from the GBT data, the zero-th (integrated brightness temperature, top center) and the first (LSR velocity, top right) ^{12}CO(2→1) moment maps from APEX. The lower contour level in the HI and CO maps denote a S/N of 2.5, with the noise of the map calculated taking into account the masking applied to the cube (see appendixes of Verheijen & Sancisi 2001; Lelli et al. 2014, for details). Underneath the maps, we plot example spectra extracted from the four, beam-sized, circular regions indicated with numbered purple circles in the CO total map. These two clouds clearly show different characteristics from both a morphological and kinematical point of view. MW-C10 has strong CO emission, covering a large fraction of the observed APEX field, distributed along a filamentary-like structure. The molecular gas is spread over a quite large range of velocities, $-200\ {\rm km\,s^{-1}} \lesssim V_{\rm LSR} \lesssim -120\ {\rm km\,s^{-1}}$, and the kinematics look very complex across the field. On the contrary, MW-C13 shows only weak emission (2–$4\sigma_{\rm rms}$) in two or three molecular gas clumps, restricted to a relatively small velocity range, $-220\ {\rm km\,s^{-1}} \lesssim V_{\rm LSR} \lesssim -200\ {\rm km\,s^{-1}}$. MW-C10 and MW-13 represent two extremes in our sample, with most of the other clouds having morpho-kinematics characteristics in between. Moment maps for all the clouds detected in this study can be found in Appendix A.

3.2. Decomposition into CO clumps

Having determined the regions with CO emission in each field, the next step was to identify clumpy molecular gas cores and to derive their physical properties. To this end we made use of PYCPROPS, an algorithm broadly used for the segmentation and the analysis of resolved molecular clouds both in the MW and in nearby galaxies. PYCPROPS identifies distinct local maxima in a spectral cube and assigns them to different clouds/clumps. Maxima identification is performed through the ASTRODENDRO package, which uses a dendogram representation (Rosolowsky et al. 2008) of the emission within the mask $\mathcal{M}(x, y, z)$. These maxima are then used as a seed for a watershed algorithm that uniquely assigns remaining pixels within the mask (i.e., fainter emission) to a identified peak based on neighboring criteria (see Rosolowsky & Leroy 2006; Rosolowsky et al. 2021, for details).

For most of our data, we used a standard set of parameters for cloud decomposition. All pixel clusters assigned by the dendogram algorithm to local maxima were required to have a $2\sigma_{\rm rms}$ contrast against the local noise level (DELTA parameter) and to cover a number of pixels at least equal to half size of beam (MINPIX = 6 pixels). A minimum separation of 45″ (FRIENDS = 5 pixels) and 2 ${\rm km\,s^{-1}}$ (SPECFRIENDS = 4 channels) between different clumps was also required. Finally, we set a COMPACTNESS parameter (Neubert & Protzel 2014) of 100, as a tradeoff between the need of identifying both compact and slightly extended molecular clumps. A visual inspection of the resulting decompositions showed that these parameters are appropriate for the majority of our clouds. However, for the most complex and filamentary molecular structures (MW-C2, MW-C10 and MW-C15), we had to tweak the above parameters, slightly increasing the DELTA and MINPIX parameters. This was necessary to avoid an excessive breaking down of the emission in these structures.

Figure 3 shows the results of the clump decomposition for three clouds of increasing emission complexity: MW-C7_2, MW-C1 and MW-C10. Overlayed to the CO integrated intensity maps, the dashed black contours show the projected boundaries of detected clumps for each HI cloud. These projected boundaries can cross each other in the 2D map as the clumps have different velocities in the spectral cube. As is shown in the figure, PYCPROPS efficiently segments the emission in data where the emission is clearly clumpy and fairly regular, like in MW-C1. For the few clouds with a more complex morphology and/or kinematics, such as the case of MW-C10, the algorithm still produces an acceptable decomposition. However, it is problematic to clearly define the boundaries between clumps in some regions where the emission morphology looks more similar to a filament than to a compact clump.

Most of the 16 HI clouds detected in CO have only a few (5–10) distinct molecular gas clumps each, like in the examples shown in the first two panels of Figure 3. Instead, the three most complex clouds in our sample (MW-C2, MW-C10, and MW-C15) reach between 20 and 30 segmented molecular gas clumps.

3.3. Physical properties of CO clumps

Some important physical properties were calculated by PYCPROPS for each molecular clump separately. These include the position and velocity centroid, linewidths, size, orientation and CO integrated intensity, and luminosity. Here we summarize how these quantities were estimated from the data (for details, we refer to Rosolowsky & Leroy 2006).

The position and central velocity of a clump are simply its intensity-weighted mean along the two spatial dimensions (right ascension and declination) and along the spectral dimension, respectively. The velocity dispersion, $\sigma_{\rm v}$ (line width), is the square root of the intensity-weighted variance in the spectral direction (i.e., the second moment), taken over all the voxels that belong to a clump. The cloud size and orientation were calculated from the intensity-weighted second moments over the two spatial axes: the major and minor axes, $\sigma_{\rm maj}$ and $\sigma_{\rm min}$, and the position angle, ϕ, of the emission distribution are determined from the diagonalization of the spatial variance-covariance matrix. The measured cloud radius was then calculated as $R = \eta \sqrt{\sigma_{\rm maj}\sigma_{\rm min}}$, where we assumed the classic value of $\eta = 1.91$ from Solomon et al. (1987). Red ellipses in Figure 3 show an example of the approximated elliptical representation of the segmented clumps, given by the measured $\sigma_{\rm maj}$, $\sigma_{\rm min}$, and ϕ.

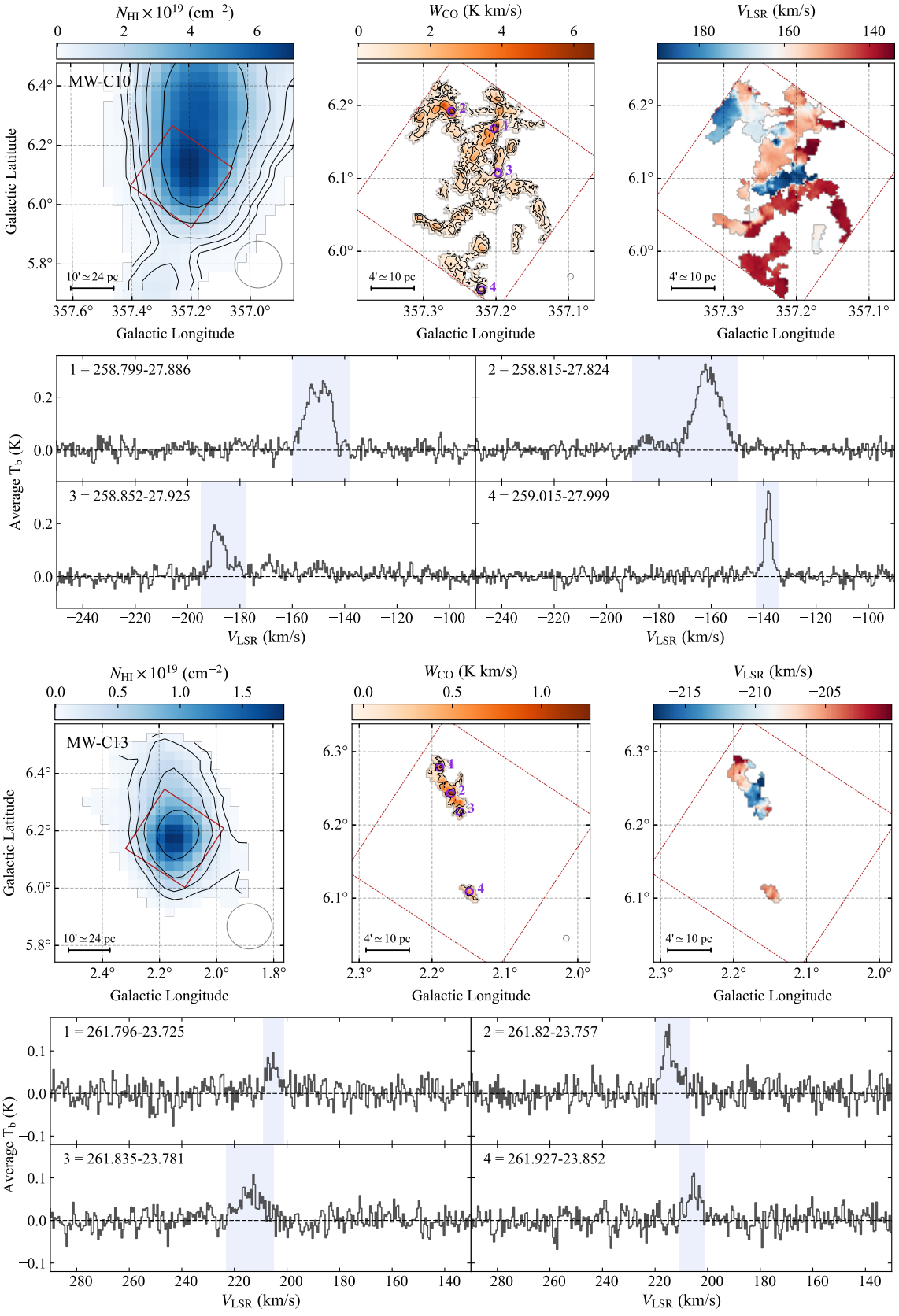

Fig. 2. Moment maps and example spectra for two clouds (MW-C10 and MW-C13). For each cloud, we show the HI column density map (*left*, blue color-scale) from GBT data, the CO total intensity map (*center*, orange color-scale) and the CO velocity map (*right*, spectral color-scale). The red squares denote the field observed in CO with APEX. Beam sizes for the GBT and APEX data are indicated as gray circles in the bottom right corner of the HI and CO maps, respectively. Spectra are extracted from the positions indicated on the CO total maps, with radius equal to the APEX beam size. Shaded blue bands in the spectra denote the velocity range of the detection. Contour levels in the HI and CO maps are at S/N levels of 2.5, 5, 10, 20 and 40.

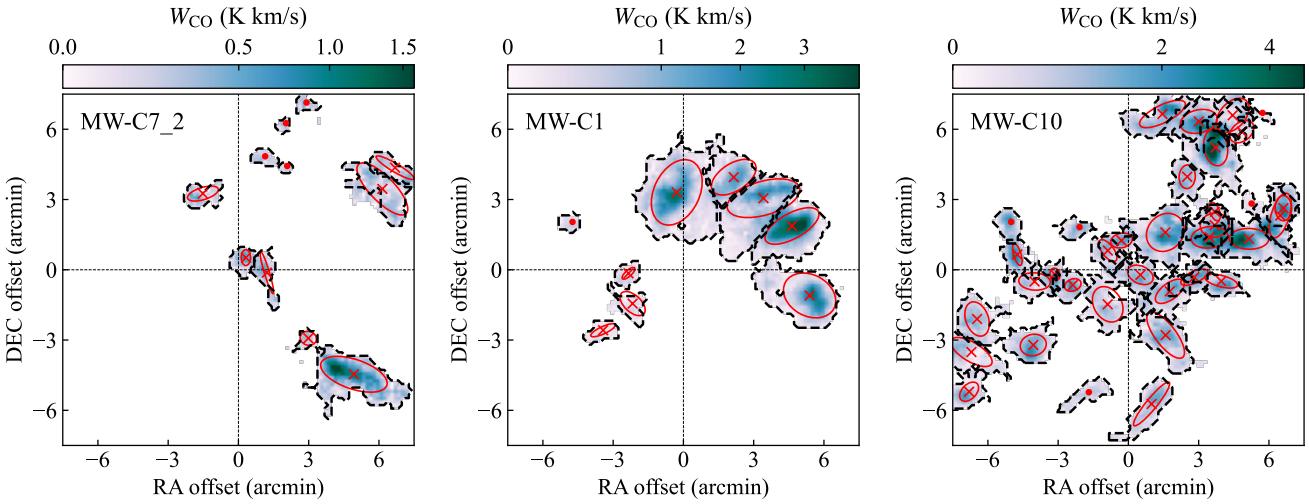

Fig. 3. Cloud segmentation for three clouds in our sample: MW-C7_2 (*left*), MW-C1 (*center*) and MW-C10 (*right*). The blue-green color maps show the masked ^{12}CO(2→1) integrated intensity maps. The dashed black contours denote the projected boundaries of each clump. The red crosses and ellipses show the emission centroid and an elliptical approximation of the emission in each clump. These ellipses represent a rough estimate of the size and orientation of the molecular clumps obtained through beam deconvolution. Clumps that could not be deconvolved are indicated as a filled dot. These clumps are not included in the analysis.

Finally, the CO luminosity of a given clump, C, is:

$$\frac{L}{[\mathrm{K\ km\,s^{-1}\,pc^2}]} = \frac{D^2}{[\mathrm{pc^2}]} \sum_{i\in C} \frac{T_i\,\Delta x\,\Delta y\,\Delta v}{[\mathrm{K\ km\,s^{-1}}]} = \\ = \frac{A_{\mathrm{pix}}}{[\mathrm{pc^2}]} \sum_{i\in C} \frac{T_i\,\Delta v}{[\mathrm{K\ km\,s^{-1}}]}, \tag{1}$$

where $A_{\mathrm{pix}} \simeq (D^2\,\Delta x\,\Delta y)$ is the physical size of a pixel in pc^2, Δx and Δy are the pixel sizes in radians (9″ for CO APEX data and 115″ for HI GBT data) and D = 8200 pc is the distance to the GC. T is the brightness temperature in K and Δv is the velocity width of a channel in km s^{-1}, and the sum is taken over all voxels in the clump.

Uncertainties on the derived properties were calculated through a bootstrapping method, whereby several trial clouds were generated from the original cloud data and parameters were recomputed for each trial cloud. In particular, for this work, we used 5000 realizations and calculated the parameter values and their uncertainties as the mean and standard deviation of the resulting parameter distributions. Finally, PYCPROPS also takes into account biases introduced by the limited sensitivity and resolution of the observations. Some measured properties, such as the spatial second moments and the luminosity, are extrapolated to correct for the missed flux due to the S/N clipping applied during cloud decomposition. Moreover, spatial and spectral resolutions have an effect on the estimates of the cloud size and line width, respectively. The rms beam size, σ_{beam}, was subtracted in quadrature from the extrapolated spatial moments to obtain "deconvolved" quantities. In a similar way, the equivalent Gaussian width of a channel is subtracted in quadrature from the extrapolated velocity dispersion.

3.4. Neutral and molecular gas masses

Masses of neutral and molecular gas were estimated from the HI and ^{12}CO(2→1) line emission, respectively. For 3D emission line data, $T(x, y, v)$, the gas column density, $N(x, y)$, at a sky position (x, y) can be written as

$$\frac{N(x,y)}{[\mathrm{cm^{-2}}]} = \frac{X}{[\mathrm{cm^{-2}\,(K\ km\,s^{-1})^{-1}}]} \sum_{v\in C} \frac{T(x,y)(v)\,\Delta v}{[\mathrm{K\ km\,s^{-1}}]}, \tag{2}$$

where the sum is taken over all velocity channels belonging to the clump C at the position (x, y). The constant X for the neutral gas emitting in HI is $X_{\mathrm{HI}} = 1.82 \times 10^{18}$ cm^{-2} (K km s^{-1})$^{-1}$, under the reasonable assumption that the gas is optically thin (e.g., Roberts 1975). For molecular gas emitting CO lines, the constant X_{CO} is known as the CO-to-H_2 conversion factor (e.g., Bolatto et al. 2013). Our choice for the X_{CO} is based on radiative transfer modeling and is discussed extensively in Section 4.

The total "luminous" mass of gas will then be

$$\frac{M}{[\mathrm{M_\odot}]} = 1.36\,\frac{m}{[\mathrm{M_\odot}]}\,\frac{D^2}{[\mathrm{cm^2}]} \sum_{(x,y)\in C} \frac{N(x,y)\,\Delta x\,\Delta y}{[\mathrm{cm^{-2}}]} \\ = \frac{\alpha}{[\mathrm{M_\odot\,(K\ km\,s^{-1}\,pc^2)^{-1}}]}\,\frac{L}{[\mathrm{K\ km\,s^{-1}\,pc^2}]}, \tag{3}$$

where the sum is made over the spatial pixels of a cloud, m is either the mass of atomic or molecular hydrogen for atomic or molecular gas and the factor 1.36 is to take into account helium. The last part of Eq. (3) is obtained by using Eqs. (1–2). The constant $\alpha = 1.36\,m\,X$ has the meaning of a mass-to-light ratio and converts the line luminosity, L, to a mass.

For all CO clumps isolated in each HI cloud, we calculated the luminous masses from the CO luminosity. Unfortunately, the significantly coarser spatial resolution of our HI GBT data (570″ vs. 28″) prevents us from comparing the atomic and molecular gas contents for each single clump. High-resolution interferometric HI observations currently exist only for two clouds with detected CO emission (MW-C1 and MW-C2, Noon et al. 2023). Therefore, for each cloud, we calculated the HI mass over the entire field covered by the APEX observations and we compared it to the total molecular gas mass in the same region. For the seven clouds with no CO detections, we estimated a molecular gas upper limit in the following way: we assumed the existence

of at least one molecular clump with a line peak at $3\sigma_{\rm rms}$ and emission spread over a 3D Gaussian having spatial FWHMs equal to the beam size and the spectral dispersion set to 2 km/s (4 channels). We highlight that this should be a quite conservative upper limit, given that such a clump would be detectable with our procedure, although barely.

4. Radiative transfer modeling and $X_{\rm CO}$

Converting the CO observed brightness temperature to a molecular mass for a cloud in a galactic wind environment is not a trivial matter. Unlike regular molecular clouds in galactic disks, the dynamical and chemical state of molecular gas in an outflow are unconstrained and we cannot simply apply the usual Galactic conversion factor of $X_{\rm CO(1\rightarrow0)} = 2\times10^{20}$ cm^{-2} (K km s^{-1})$^{-1}$ (e.g., Bolatto et al. 2013). Our early observations of three clouds in the wind (Di Teodoro et al. 2020; Heyer et al. 2025) have also suggested a wide range of possible $X_{\rm CO}$ for these objects.

For this work, we used the radiative transfer software DESPOTIC (Derive the Energetics and SPectra of Optically Thick Interstellar Clouds, Krumholz 2014) to explore the range of physically motivated conversion factors for clouds in a wind. DESPOTIC calculates the thermal and chemical equilibrium state of an optically thick cloud subject to a given interstellar radiation field χ and a given cosmic-ray ionization rate ζ. To compute the chemical equilibrium, we adopted the H–C–O chemical network by Gong et al. (2017), varying the dust abundance $Z_{\rm dust}$ from solar to super-solar values. In the thermal balance, DESPOTIC takes into account photoelectric heating from dust grains, heating by cosmic rays, and turbulent heating, while cooling is due to common atomic and molecular transitions (including HI, CII, CI, OI, and CO) and energy transfer via collisions between gas and dust. Level populations were computed using an escape probability approach, where the escape probabilities were derived based on DESPOTIC's assumption of spherical cloud geometry.

We approximated a molecular clump as a single-zone spherical cloud described by three parameters: its hydrogen number density, $n_{\rm H}$, column density, $N_{\rm H}$, and turbulent (i.e., nonthermal) velocity dispersion, $\sigma_{\rm turb}$. For a given set of cloud parameters ($n_{\rm H}$, $N_{\rm H}$, $\sigma_{\rm turb}$) and environmental parameters (χ, ζ, $Z_{\rm dust}$), DESPOTIC computes the equilibrium state and returns the final thermodynamical/chemical quantities (e.g., gas temperature, H_2/HI volume and column densities, abundances of the different species). It also estimates the integrated brightness temperatures for the tracked species, for example ^{12}CO and ^{13}CO, and for different line transitions, for example $1\rightarrow0$ and $2\rightarrow1$. We performed these calculations on a $50\times50\times5\times4\times4\times3$ six-dimensional grid, exploring both the cloud and the environment parameter spaces. In particular, we explored clouds with number densities of $n_{\rm H}$ = 1–10 000 cm^{-3}, column densities of $N_{\rm H} = 10^{19}$–10^{23} cm^{-2}, and velocity dispersions of $\sigma_{\rm turb}$ = 1–10 km s^{-1}. We also explored different environments, varying the interstellar radiation field, χ, and the cosmic-ray ionization rate, ζ. The former was varied between $0.1\chi_0$ and $1000\chi_0$, where χ_0 is the standard solar radiation field (Draine 1978), and the latter between 10^{-17} s^{-1} and 10^{-14} s^{-1}. We remind the reader that observations in the solar neighborhood found that the ionization rate is 10^{-16}–10^{-17} s^{-1} in diffuse and dense clouds, respectively, with quite a large dispersion around these values (e.g., Padovani et al. 2020), while estimates in the CMZ span an even wider range, from $\sim10^{-14}$ s^{-1} (Oka et al. 2019) to values not vastly different from those in the solar neighborhood (Ginsburg et al. 2016; Krumholz et al. 2023) and to values intermediate between these two (Armillotta et al. 2020). We consider dust abundances ($Z_{\rm dust}$) equal to one, two, and three times the solar value. With our choice of χ, ζ, and $Z_{\rm dust}$, we aim to probe a wide range of possible environments, from subsolar to highly super-solar, to overcome our ignorance on the actual ambiance experienced by the clouds. On the one hand, because they are at GC and above the CMZ, we may expect a more extreme environment than the solar neighborhood. On the other hand, our CO clouds do not lie in the Galactic disk, but are a few hundred parsecs to 2 kpc from it; because both the radiation field and the ionization rate are expected to drop with distance from the plane, models with intermediate χ and ζ might be more representative of the conditions in the wind. The full parameter space explored with DESPOTIC is summarized in Table 2.

Table 2. Range of cloud and environmental parameters explored in the radiative transfer modeling with DESPOTIC.

Parameter	Range or values
$\log(n_{\rm H}/{\rm cm}^{-3})$	[1–4] with 50 steps of 0.06 dex
$\log(N_{\rm H}/{\rm cm}^{-2})$	[19–23] with 50 steps of 0.08 dex
$\sigma_{\rm turb}/{\rm km\,s}^{-1}$	[1, 3, 5, 7.5, 10]
$\log(\chi/\chi_0)$	[-1, 0, 1, 2]
$\log(\zeta/{\rm s}^{-1})$	[–17, –16, –15, –14]
$Z_{\rm dust}/Z_\odot$	[1, 2, 3]

Figure 4 illustrates an example of outputs from DESPOTIC on the $\log(n_{\rm H})-\log(N_{\rm H})$ grid for a model with $\sigma_{\rm turb}$ = 3 km s^{-1}, $\chi=\chi_0$, $\zeta = 10^{-16}$ s^{-1} and $Z_{\rm dust}=Z_\odot$. The first row shows the predicted H_2 and HI column densities and abundances: as was expected, moving from low- to high-density clouds, the fraction of H_2 increases, while that of HI decreases. In this particular environment condition, a cloud is always fully molecular for $\log(n_{\rm H}/{\rm cm}^{-3})\gtrsim2.5$. In the second row, we plot the gas temperature, the CO abundance, the integrated brightness temperature $W_{\rm CO(2-1)}$ for the ^{12}CO(2→1) line and the corresponding conversion factor $X_{\rm CO(2-1)} = N_{\rm H_2}/W_{\rm CO(2-1)}$, where the H_2 column density was calculated as $N_{\rm H_2} = x_{\rm H_2}N_{\rm H}$, with $x_{\rm H_2}$ being the H_2 abundance per hydrogen nucleus. From the last plot, we can notice that $X_{\rm CO(2-1)}$ spans over more than five orders of magnitude. However, we can further constrain the $X_{\rm CO(2-1)}$ parameter space by using some observed properties of our data: in particular, the HI column densities calculated from the HI data through Equation (2), the $W_{\rm CO}$ measured from the CO data and the cloud radius $R = 3/4\,n_{\rm H_2}/N_{\rm H_2}$ obtained from the clump decomposition. For example, the black contour on the $X_{\rm CO(2-1)}$ plot denotes the allowed parameter space after we impose the observed properties of clumps in MW-C1, i.e., $0.5 < W_{\rm CO}/({\rm K\,km\,s}^{-1}) < 4$, $19 < \log(N_{\rm HI}/{\rm cm}^{-2}) < 21.5$ and $R < 4$ pc. Thus, for this particular model and observed cloud, the range of allowed $X_{\rm CO(2-1)}$ is reduced to $8\times10^{20} - 5\times10^{21}$ cm^{-2} (K km s^{-1})$^{-1}$.

For each cloud in our sample, we selected the closest models in terms of $\sigma_{\rm turb}$ and we imposed the observational clump measurements in $W_{\rm CO}$, R, and $N_{\rm HI}$. Adding up all the allowed values from all the models of the different environments, we built up distributions of $X_{\rm CO}$ for each cloud in the wind. From these $X_{\rm CO}$ distributions, which are fairly log-normal, we take

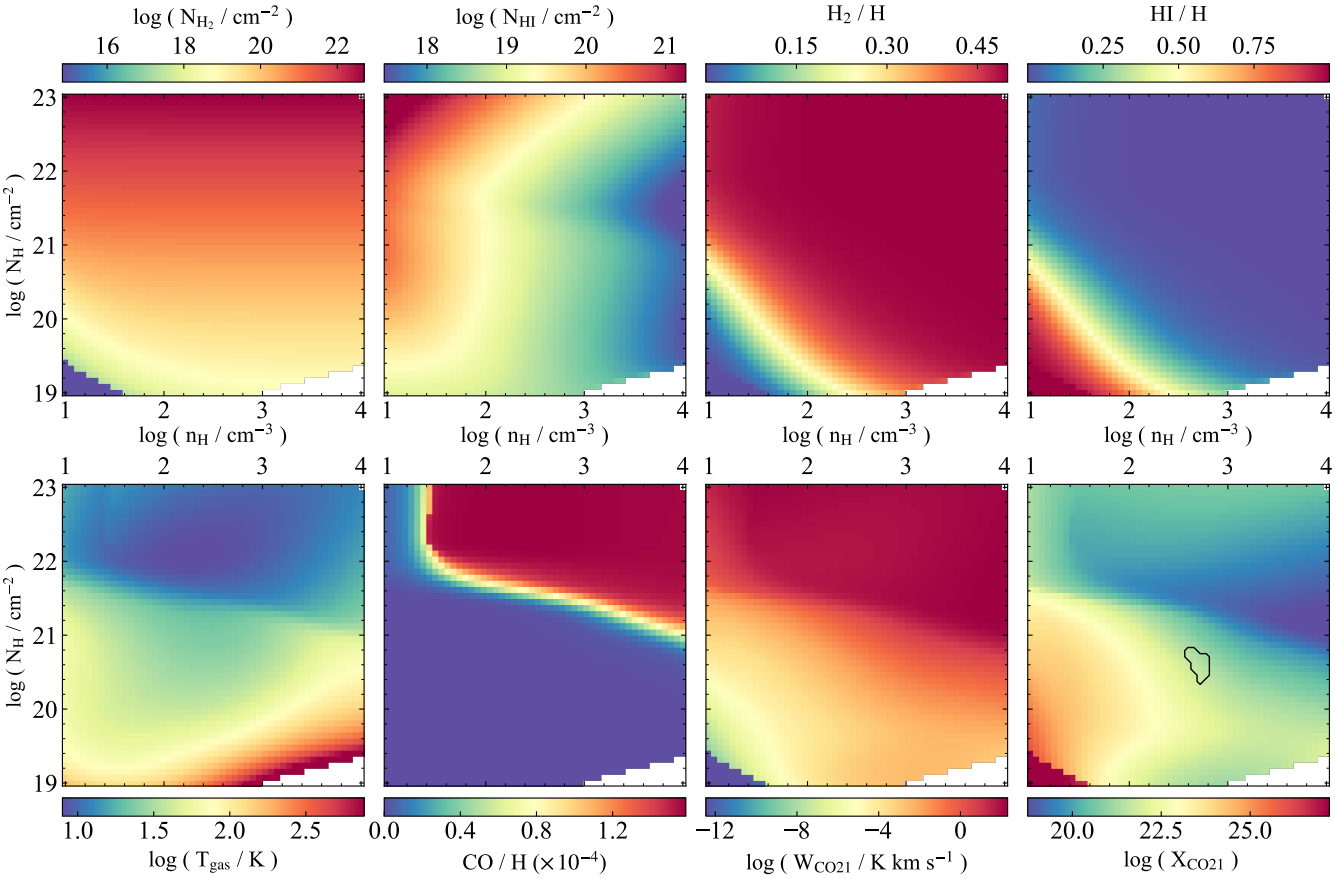

Fig. 4. DESPOTIC results for a model with σ_{turb} = 3 km s^{-1}, $\chi = \chi_0$, $\zeta = 10^{-16}$ s^{-1} and solar dust abundance. Top panels, from left to right: predicted H_2 column density, HI column density, H_2 and HI abundances per H nucleus. Bottom panels, from left to right: Gas temperature, CO abundance per H nucleus, integrated brightness temperature and CO-to-H_2 conversion factor for the ^{12}CO(2→1) emission line. Blank pixels denote regions of the grid where the models did not converge. The black contours on the X_{CO} plot represent an example of the constraint on the parameter space given by our data for MW-C1. Similar radiative-transfer models are used to calculate fiducial conversion factors within each HI cloud.

the 50th percentile as the fiducial value and the 15.87th and 84.13th percentiles as lower and upper uncertainty bounds. This approach returns central values of $X_{CO(2-1)}$ in the range 6–20×10^{20} cm^{-2} (K km s^{-1})$^{-1}$, several times larger than the typical Galactic conversion factor. We used these values to calculate molecular masses for each CO clump, propagating the asymmetric errors with a Monte Carlo method.

Finally, we stress that our approach is model-dependent and relies on the assumption of thermal and chemical equilibrium, which may not apply to clouds entrained in galactic winds (see discussion in Section 6.4). Noon et al. (2023) showed that at least two of our clouds (MW-C1 and MW-C2) have atomic shielding layers too thin to maintain chemical equilibrium. Nonequilibrium abundances can cause values of X_{CO} somewhat higher than those found in equilibrium, because when a cloud undergoes a rapid reduction in shielding (for example because its outer layers are stripped off as it is entrained into a wind), the resulting increase in UV flux affects the CO and H_2 on different timescales. The CO will rapidly find a new equilibrium when exposed to an increased radiation field, while self-shielding effects mean that it takes finite time for the increased photon flux to dissociate the H_2 and drive its abundance to a new, lower equilibrium. During this adjustment period, the CO luminosity is reduced, but the H_2 abundance has not yet caught up, increasing X_{CO}, though the strength of this effect is still under investigation (Noon et al., in prep.).

5. Results

5.1. Observed properties

Our cloud decomposition method detected a total number of 207 molecular gas clumps within the 16 high-velocity HI clouds with CO detections. As was mentioned in Section 3.2, most HI clouds have fewer than ten segmented molecular clumps, but some of the most complex structures can show up to a few dozens clumps (e.g., MW-C10). Figure 5 shows the distributions of some of the molecular clump properties: from left to right, we plot histograms of clump radii, line widths (velocity dispersion) and CO luminosities. Detected clumps are compact, with typical sizes of 1–3 pc, and a median value of 1.2 pc. They show velocity dispersions up to $\sigma_v \simeq 6$ km s^{-1}, with a median value of 2 km s^{-1}, larger than the expected thermal broadening for a typical molecular cloud ($\lesssim 1$ km s^{-1} for a temperature $T \lesssim 1000$ K), suggesting a significant level of turbulent broadening. Their CO luminosity ranges from 0.3 to 30 K km/s pc^2, which is faint compared to regular clouds in the disk where CO luminosities range from 10 to 10^6 K km/s pc^2 (Miville-Deschênes et al. 2017, MD17 hereinafter).

5.2. Scaling relations

Molecular clouds in the MW and in nearby spiral galaxies are known to lie on scaling relations between their most important

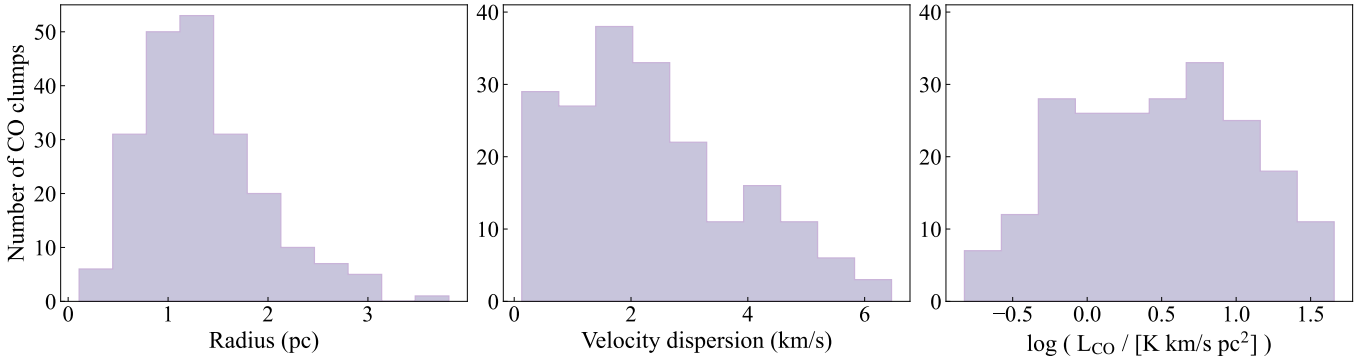

Fig. 5. Histogram distributions of the observed properties of the molecular clumps detected in the APEX data. From left to right: Cloud radius (assuming a distance of 8.2 kpc), velocity dispersion, and ^{12}CO(2→1) luminosity (Equation (1)).

physical properties, namely radius, velocity dispersion, and mass (e.g., Solomon et al. 1987; Rosolowsky et al. 2021; Deng et al. 2025). We investigate whether the clumps defined in our study still obey the same relations. The top row of panels of Figure 6 illustrates these scaling laws for our cloud sample (colored points based on parent HI cloud) compared to the MW disk measurements (gray dots) from MD17. In these plots, we also include the cloud MW-C21 detected in the ^{12}CO(1→0) line by Heyer et al. (2025) (dark gray triangles), after reanalyzing the LMT data with the same methods used for our APEX data for consistency. From left to right, we show the velocity dispersion–radius relation ($\sigma_v - R$), the luminous mass–radius relation (M_{mol}–R) and the luminous mass–velocity dispersion relation (σ_v–M_{mol}). Full black lines denote the best-fit relations to the disk sample, indicated in the caption.

Wind molecular clumps closely follow the M_{mol}–R relation (panel b) of disk molecular clouds, extending the power law to the low-mass small-radius regime. Radius and mass are clearly correlated quantities for our sample, with a Spearman rank-order correlation coefficient of $\rho \sim 0.7$ (with 1 indicating perfect monotonically increasing correlation and 0 no correlation). We note that the choice of conversion factors, based on DESPOTIC modeling, is key to bringing our clouds onto the relation. Had we used a standard Galactic X_{CO}, the wind clouds would have lain about an order of magnitude below the relation. The fact that wind clouds lie on the mass–size relation ($M_{mol} \propto R^2$) indicates that these objects have nearly constant average surface densities that do not depend on R, which also implies that $n_{H_2} \propto R^{-1}$ (e.g., Larson 1981). This is also a general, well-known feature of molecular clouds in the MW disk (e.g., Roman-Duval et al. 2010; Chen et al. 2020; Lewis et al. 2022). The intercept of the relation implies an average surface density of ~40 $M_\odot$ pc^{-2}, which for solar dust abundances corresponds to a visual extinction A_V of a few magnitudes, roughly the extinction theoretically predicted to be necessary to shield CO molecules from photodissociation by the interstellar radiation field (Bolatto et al. 2013). Thus the fact that the wind and Galactic plane molecular clumps both feature constant surface densities of this value likely reflects that for both classes of object the edge of the CO-bright region is determined by the common physics of photodissociation.

Unlike the M_{mol}–R relation, the clumps do not follow neither the σ_v–R (panel a in Figure 6) nor the σ_v–M_{mol} (panel c) relation of disk clouds: in both cases, wind clouds have larger velocity dispersions than regular molecular clouds, and lie well above the relations, in a region populated by only a handful disk clouds. The σ_v–R relation is the only one based on pure observational measurements (modulo an assumed distance), and does not depend on our choice of X_{CO}, which is model dependent and remains the greatest source of uncertainty. The σ_v–R plane for disk clouds is known to show a large scatter and a relatively low correlation coefficient (see e.g., the reviews by Hennebelle & Falgarone 2012; Heyer & Dame 2015). For our wind sample of clumps, we also find a large scatter and a Spearman coefficient $\rho \sim 0.2$, indicating a very marginal positive correlation between radius and velocity dispersion, compared to a $\rho \sim 0.5$ for the disk sample. Similarly, the σ_v–M_{mol} plane for wind clouds also shows a similar weak correlation ($\rho \sim 0.3$ compared to $\rho \sim 0.7$ for MW disk clouds).

5.3. Velocity dispersion and turbulence

The large velocity dispersion of our sample suggests a higher level of turbulence in clouds in the wind with respect to clouds in the disk. A useful parameter in this context is the velocity dispersion normalized at 1 pc, $\sigma_0 = \sigma_v/(R/[1\,\mathrm{pc}])^\gamma$, which basically represents the typical amplitude of turbulent motions on a parsec scale. The exponent γ is related to the nature of the turbulence, $\gamma = 1/3$ for subsonic turbulence and $\gamma = 1/2$ for supersonic turbulence. Assuming the latter, we find a mean $\sigma_0 \simeq 2$ km s^{-1} for our sample, a number that is at least three times larger than in typical molecular clouds in the disk ($\sigma_0 \sim 0.4$–0.8 km s^{-1}, e.g., Solomon et al. 1987, MD17).

Finally, we can estimate the internal (turbulent) pressure experienced by the clumps as

$$\frac{P_{int}}{k} = \frac{\mu m_H}{k} n_{H_2} \sigma_v^2 = \frac{3 M_{mol} \sigma_v^2}{4\pi k R^3}, \quad (4)$$

where k is the Boltzmann constant, m_H the hydrogen mass, and μ the molecular weight. Our wind clumps have turbulent pressures $P_{int}/k \sim 10^4$–10^7 K cm^3. Molecular clouds in the MW disk have also a wide range of pressures, mostly between 10^3–10^6 K cm^3, with the highest P_{int} found in the central kpc of the Galaxy and a decreasing trend as a function of Galactocentric radius (MD17).

5.4. Virial ratio and clump boundedness

Given the high internal pressures, one may wonder whether these clouds in the wind are gravitationally bound or not. A broadly used approach to investigate this makes use of the "virial" mass, i.e., the mass that a self-gravitating molecular cloud should have if it was in virial equilibrium. For a cloud with a spherical volume density profile $\rho(r) = r^{-\beta}$ and no magnetic support nor

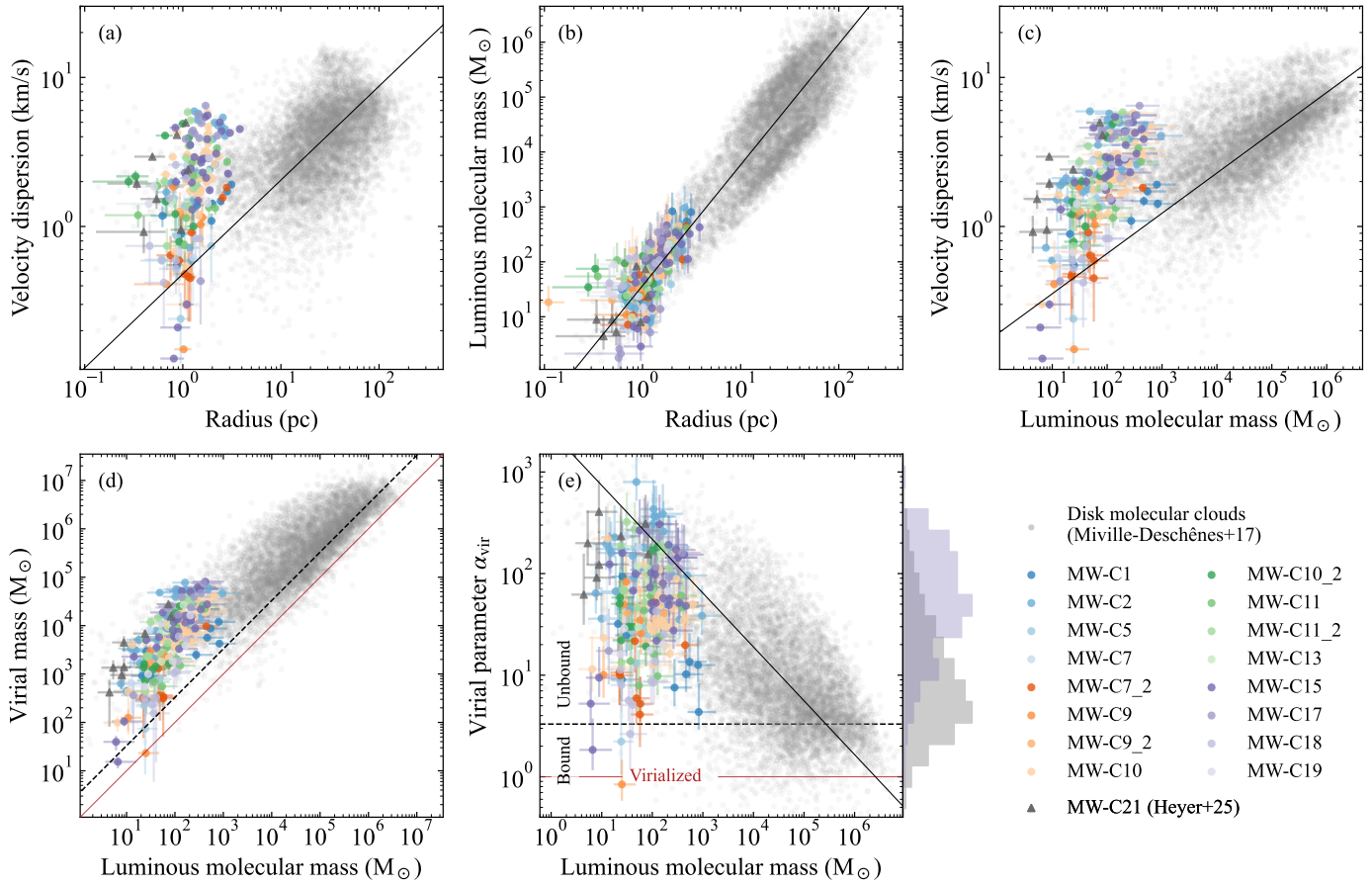

Fig. 6. Scaling relations of molecular clouds in the MW wind compared to molecular clouds in the MW disk. In all panels, gray dots indicate the MW disk sample from MD17, the points are the wind clumps studied in this paper from APEX data, color-coded by their parent HI cloud, while the dark gray triangles are for the MW-C21 cloud from LMT data (Heyer et al. 2025). Full black lines denote the best-fit relations to the disk sample from MD17. Panel (a) σ_v–R relation, best-fit $\sigma_v = 0.48R^{0.63}$; (b) M_{mol}–R relation, best-fit $M_{mol} = 36.7R^{2.2}$; (c) σ_v–M_{mol} relation, best-fit $\sigma_v = 0.19M_{mol}^{0.27}$; (d) M_{vir} vs. M_{mol}; (e) α_{vir} vs. M_{mol}, best-fit $\alpha_{vir} = 2500M_{mol}^{-0.53}$. In panels (d) and (e), the full red line denotes a virialized cloud ($M_{mol} = M_{vir}$), while the dashed black line indicates the $\alpha_{vir} = 3.3$ boundary between gravitationally bound and unbound clouds. The histograms on the y axis of panel (e) show normalized distributions of α_{vir} marginalized over M_{mol} for disk clouds (gray) and wind clouds (purple). The extremely large virial parameters, driven by the large velocity dispersions, imply that the clouds are not gravitationally bound.

pressure confinement, the virial mass can be written as (Solomon et al. 1987)

$$M_{vir} = \frac{3(5-2\beta)}{(3-\beta)} \frac{R\,\sigma_v^2}{G}, \tag{5}$$

where G is gravitational constant. In this work, we assume $\beta = 1$ based on the findings of the M_{mol}–R relation and for consistency with previous studies, which leads to the well known $M_{vir,[M_\odot]} \simeq 1040\,R_{[pc]}\,\sigma^2_{v,[km/s]}$. We note however that Eq. (5) depends only weakly on the chosen value of β. Deviations from virialization can be studied through the so-called virial parameter α_{vir}, which roughly corresponds to the ratio of total kinetic energy to gravitational energy (Bertoldi & McKee 1992):

$$\alpha_{vir} = \frac{3(5-2\beta)}{(3-\beta)} \frac{R\,\sigma_v^2}{GM} = \frac{M_{vir}}{M_{mol}}. \tag{6}$$

Gravitationally bound objects have $\alpha_{vir} \sim 1$; large ratios, i.e., $\alpha_{vir} \gg 1$, indicates that there is an excess of kinetic energy and thus a cloud would expand and possibly dissipate without further confinement; $\alpha_{vir} \ll 1$ suggests that a cloud would collapse without further support.

In the bottom panels of Figure 6, we show plots of luminous molecular mass versus virial mass (left) and of virial parameter versus luminous mass (right) for our cloud sample. Full red lines denote $M_{mol} = M_{vir}$, i.e., the locus of virialized clouds. Most of our clouds have virial masses that exceed their luminous molecular mass by more than an order of magnitude, with corresponding virial parameters ranging from a few to several hundred. This is mainly driven by the higher than usual velocity dispersions, as was discussed in the previous section. Nonetheless, they seem to mildly follow the general trend, seen also in disk clouds, of a larger α_{vir} for low-mass clouds.

In these plots, dashed black lines represent $\alpha_{vir} = 3.3$, which approximately indicates the equilibrium between kinetic and gravitational energy (see Appendix D in MD17, for details): clouds above (below) this line have more (less) kinetic than gravitational energy and can therefore be considered gravitationally unbound (bound). While most of the molecular mass in the MW disk is confined within clouds that are either bound or loosely unbound ($\alpha_{vir} \lesssim 10$), the vast majority (nearly 90%) of wind clouds appear strongly unbound ($\alpha_{vir} \gg 10$–100). This can be appreciated by looking at the α_{vir} distributions for wind clouds (purple histograms) and disk clouds (gray), plotted in panel (e) of Figure 6. These characteristics make the wind clouds more

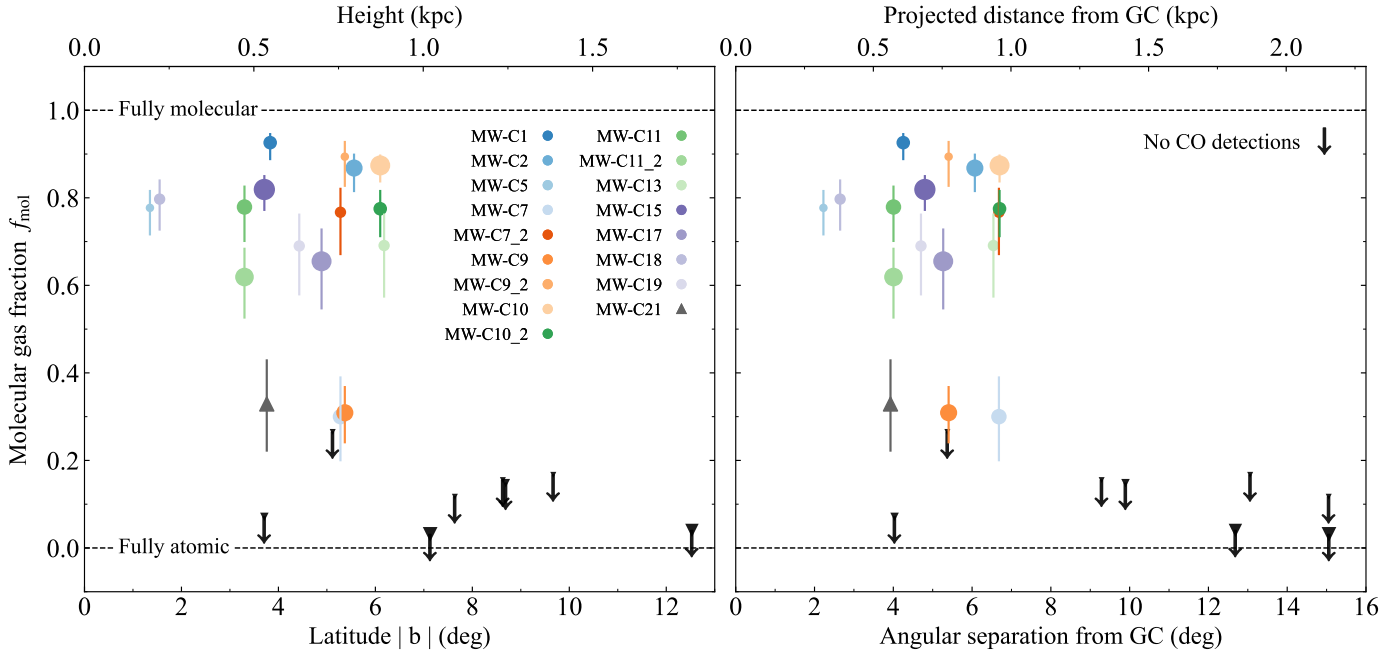

Fig. 7. Molecular gas fraction as a function of latitude or height (left panel) and as a function of angular separation or projected distance from the GC (right panel). Points denote the CO detections, color-coded as in Figure 6. Up-down triangles with arrows represents observed HI clouds with no CO detections, for which we estimate molecular mass upper limits (see Section 3.4). The size of all markers is proportional to the peak HI column density of the cloud, ranging from 5×10^{18} cm^{-2} to 8×10^{19} cm^{-2}.

similar to giant molecular clouds observed in galaxy centers (Rosolowsky et al. 2021) and high-velocity molecular clouds (Nagata et al. 2025) of external galaxies.

5.5. Molecular mass fraction and evolution with latitude

For each HI cloud with a CO detection, we calculated the molecular gas mass fraction, f_{mol}:

$$f_{mol} = \frac{\sum_i M^i_{mol}}{\sum_i M^i_{mol} + M_{at}}, \quad (7)$$

where M_{at} is the atomic gas mass derived from the GBT HI data in a region coincident with the APEX field (thus not in the entire HI cloud), and the sum for the molecular mass is taken over all the detected clumps in a HI cloud. We calculated the fraction globally for each HI cloud because, as was mentioned in Section 3.4, the mismatch between the spatial resolutions of GBT and APEX prevents us from calculating it clump by clump. For HI clouds with no CO detections, we calculated an upper limit on the detectable molecular gas mass (see Section 3.4), which translates into an upper limit on f_{mol}. Most of our clouds with CO emission have very high molecular gas fraction, $f_{mol} = 0.6$–0.9, meaning that 60% to 90% of the total gas mass is in the molecular phase. Only two clouds (MW-C7 and MW-C9) show lower gas fractions of $f_{mol} = 0.3$. The higher molecular fractions reported here, compared to those found in the previous works by Di Teodoro et al. (2020) and Heyer et al. (2025), are due to the larger X_{CO} values adopted in this work. A table with our derived masses and molecular gas fraction can be found in Appendix B.

In a scenario in which cold gas is lifted up from the disk and entrained within the hot wind, we might expect the properties (R, σ_v and f_{mol}) of the cold clouds to evolve with time and distance from the GC, due to the combination of dynamical interaction between the hot and the cooler phases and photodissociation (Vijayan & Krumholz 2024). However, in our sample we see no clear signature of an evolution with distance of the observed clump parameters. In particular, Figure 7 shows the evolution of the molecular gas fraction as a function of latitude or height (left panel) and angular separation or projected distance from the GC (right panel). Markers and colors follow the convention of Figure 6, while the up-down arrows denote the upper limits corresponding to non-detections in CO. While there is no visible trend of f_{mol} with height nor distance, it is interesting to note that we have no CO detections in clouds above a latitude $|b| \gtrsim 7°$, corresponding to a distance of about 1 kpc. We note that, although the APEX subsample was selected to broadly reflect the spatial and column-density distribution of the underlying HI population, these latitude trends may still be influenced by completeness biases and should therefore be interpreted with caution. Finally, we test whether the sharp decline in molecular gas could be linked to the existence of ionization cones proposed by Bland-Hawthorn et al. (2019) (see also Sarkar 2024). In this scenario, a recent (~3 Myr) Seyfert-like burst from Sgr A* produced radiative cones that are tilted by ~15° with respect to South Galactic pole, potentially dissociating or ionizing gas within their volume. However, when examining cloud positions and molecular gas fractions as a function of angular offset from the cone axis, we find no correlation and no tendency for CO non-detections to lie near the axis.

One might expect that higher molecular gas fractions are preferentially found in clouds with higher HI column density, as a dense atomic layer should provide shielding to molecule dissociation. Yet, in our sample we find no correlation between the f_{mol} and the HI column density. This can be appreciated in Figure 7, where the size of the markers is proportional to the peak HI column density: some clouds with very high HI column densities (e.g., MW-C3 or MW-C16) have no detectable CO emission; even more puzzlingly, some clouds that are very faint

in HI show CO detections (e.g., MW-C5, MW-C14, see also Figure 1). If molecular clouds are entrained in the hot wind and gradually dissociate into atomic hydrogen (Noon et al. 2023), these cases may represent opposite stages of the evolutionary sequence. Clouds that have just become entrained may quickly lose their diffuse outer layers, stripping away much of the HI, while leaving dense molecular cores. As these cores are subsequently exposed to dissociating radiation, they are destroyed from the outside in, producing clouds rich in HI but poor in molecular gas. However, we also stress that the large beam of the GBT (570″) smears out HI emission and leads to measure lower column densities than the real ones; this beam dilution effect likely hides compact and high-density HI clumps hosting molecular gas. High-resolution interferometric HI data, matching the resolution of CO data, are essential to reliably study the relationship between neutral and molecular gas.

6. Discussion

6.1. Sources of turbulence

Our results suggest that cold molecular clouds in the MW nuclear wind have physical properties that differ from regular molecular clouds in the disk. Although they have masses and sizes generally smaller than the bulk of molecular clouds in the disk, they still lie on the mass–size relation. The most clear distinctive feature of wind clouds is their broad linewidths, generally larger than their disk counterparts at fixed size or mass, placing them well above the canonical linewidth–size relation and indicating an excess of nonthermal motions. This implies a high level of turbulence and a large internal turbulent pressure, on the order of $P/k_{\rm B} \sim 10^4$–10^7 K cm^{-3}.

One key open question is what drives the turbulence observed in these clouds. In the case of molecular clouds in the disk, several mechanisms have been proposed, such as stellar feedback, gravitational instabilities, or magnetorotational instabilities (Heyer & Dame 2015), but these are unlikely to operate in the same way in clouds embedded in a galactic wind. The clouds in our sample are typically located at heights of 0.2–1 kpc above the Galactic plane, and are therefore relatively far from active star-forming regions in the disk and their associated feedback. In addition, the absence of high-density gas tracers like HCN and HCO$^+$ in our deep APEX pointings toward some of the densest CO clumps supports the idea that these objects are diffuse and not sites of star formation. Stellar feedback is therefore an unlikely source of turbulence, suggesting that other mechanisms must be responsible. The interaction between the hot and cold phases of the outflow could be the main driver of turbulence, through compression and hydrodynamical instabilities at the interface between the two fluids. This picture is also supported by the recent findings of Gerrard et al. (2024): their analysis of the turbulence properties of MW-C1 and MW-C2 found that both clouds are in a sub-to-trans-sonic regime (Mach numbers $\mathcal{M} \simeq 1.1$–1.4) and exhibit predominately compressively driven turbulence (with a turbulence parameter $b \simeq 1$; Federrath et al. 2010), especially in the cloud's head.

6.2. Cloud confinement

Given the high internal pressure, one might expect molecular clouds embedded in the wind to expand and disperse over just a few clump crossing times. The crossing time for a cloud is approximately $t_{\rm exp} \sim R/\sigma_{\rm v}$. For a typical cloud of $R \simeq 1$ pc and $\sigma_{\rm v} = 2$ km s^{-1}, this yields an expansion timescale on the order of ∼0.5 Myr, significantly shorter than the kinematic timescale of entrainment, estimated to be ≃5–10 Myr (Di Teodoro et al. 2018; Lockman et al. 2020). For the clouds to survive over such timescales, some form of binding force must at least partially counteract their internal pressure. Our virial analysis shows that self-gravity alone is insufficient to bind the clouds, as we derive virial ratios $\alpha_{\rm vir} \gg 10$–100 for most objects in our sample.

Clumps are embedded within HI clouds, and both are entrained within the hot flow. External pressure from both these phases may help the molecular clumps to remain bound. Neutral gas can contribute with both thermal pressure, $P_{\rm th}/k = nT$, and turbulent pressure, given by Equation (4). For typical properties of the observed HI population, with temperatures in the range $T \simeq 1000$–8000 K, densities $n = 0.1$–10 cm^{-3} and velocity dispersions $\sigma_{\rm v,\,neu} \sim 5$–$10$ km/s, we expect thermal pressures of a few 10^4 K cm^{-3} and turbulent pressures of 10^4–10^5 K cm^{-3}. The physical conditions of the hot wind are more uncertain. Assuming number densities $n = 10^{-3}$–10^{-1} cm^{-3} and temperatures $T = 10^6$–10^7 K, the corresponding thermal pressures span 10^4–10^6 K cm^{-3}. In the most optimistic scenario, the total external pressure could therefore reach 10^6 K cm^{-3}, which would be sufficient to confine approximately half of the observed molecular clumps in the wind. However, achieving such high external pressures would require an extremely dense (∼0.1 cm^{-3}) and hot medium (∼10^7 K) up to distances of ≃1 kpc. These values are unlikely at these distances, as they exceed both theoretical predictions for hot winds (e.g., Chevalier & Clegg 1985; Bustard et al. 2016) and observational estimates from X-ray studies in the MW (Ponti et al. 2019; Yeung et al. 2024). A large fraction of these clouds may therefore be undergoing some degree of expansion, although in our data we do not see any strong trend in cloud radius as a function of distance from the Galactic plane. Additional confinement mechanisms, such as magnetic fields and cosmic ray pressure, may also be in place. These findings, based on a much larger sample of molecular clumps, fully confirm and strengthen the results of Heyer et al. (2025), who reached similar conclusions for the case of MW-C21.

6.3. Molecular gas dissociation

The absence of CO detections in the six HI clouds located at distances larger than 1 kpc is also intriguing. While this may be a coincidence, if confirmed in future observations, it would suggest that molecular gas does not survive for long within the wind and is dissociated during its journey, as also proposed by Noon et al. (2023). For a cloud traveling at a constant velocity of ∼300 km s^{-1}, it would take approximately 3 Myr to reach a distance of 1 kpc, providing a rough upper limit for the molecular gas dissociation timescale. However, since most clouds at heights of 0.5–1 kpc still show very high molecular fractions ($f_{\rm mol} \sim$ 0.7–0.8), the dissociation process may occur on much shorter timescales, possibly less than 1 Myr.

One speculative explanation for the presence of the sharp transition around 1 kpc could be a change in the properties of the hot ambient medium surrounding the clouds: for instance, if the hot gas becomes significantly less dense and cooler above 1 kpc, the resulting drop in external pressure could trigger rapid cloud expansion. This expansion might enhance the cloud exposure to the radiation field and to hydrodynamical instabilities, thereby accelerating the dissociation of molecular gas. Clearly, further high-resolution observations of the neutral and molecular gas content in the MW wind are essential to develop a more comprehensive understanding of these processes.

6.4. Mass loading and molecular mass uncertainties

All the clouds with CO detections have high molecular gas fraction, ranging from 0.3 to 0.9, with a median value of 0.66. The total atomic gas mass in the entire known HI population at heights $z \leq 1$ kpc is $M_{\rm at,\,tot} \simeq 1.5 \times 10^5\,{\rm M}_\odot$. If we assume that each of these clouds has a median molecular fraction of 0.66, the total cold (molecular plus atomic) gas mass within 1 kpc adds up to $M_{\rm cold,\,tot} \simeq 3 \times 10^5\,{\rm M}_\odot$. For a timescale $t \simeq 3$ Myr to reach 1 kpc at a velocity of 300 $\rm km\,s^{-1}$, we can estimate a cold mass outflow rate of $\dot{M}_{\rm cold} = M_{\rm cold,\,tot}/\,t \simeq 0.1\,{\rm M}_\odot\,{\rm yr}^{-1}$. Given the star-formation rate of SFR $\sim 0.1\,{\rm M}_\odot$ in the CMZ (Henshaw et al. 2023), we obtain cold mass loading factors $\eta = \dot{M}_{\rm cold}/{\rm SFR}$ on the order of unity at $0 < z\,/\,{\rm kpc} < 1$. Such a cold mass-loading factor is broadly consistent with the molecular loading factors reported for nearby starbursts ($\eta \sim 0.5$–5) and lies at the lower end of the values measured in AGN-driven winds ($\eta \sim 1$–10) (see e.g., Fluetsch et al. 2019; Veilleux et al. 2020). We emphasize, however, that direct robust comparisons remain difficult, as loading factor estimates are sensitive to differences in spatial resolution, adopted assumptions (e.g., conversion factor, outflow geometry and timescale), and the physical scales over which these measurements are made.

The dominant source of uncertainty in this work lies in the conversion between the observed integrated CO flux and molecular gas mass. We attempt to constrain a range of plausible conversion factors using physically motivated models through DESPOTIC (Section 4), although these rely on assumptions that may not be fully applicable to clouds embedded in a wind (i.e., thermal and chemical equilibrium). Our modeling returns a median $X_{\rm CO21} \simeq 1 \times 10^{21}\ {\rm cm}^{-2}\,({\rm K\,km\,s^{-1}})^{-1}$ across all the HI clouds, corresponding to a median $\alpha_{\rm CO21} \simeq 22\,{\rm M}_\odot\,({\rm K\,km\,s^{-1}\,pc^2})^{-1}$, which is about three times higher than the canonical Galactic value of $6.7\,{\rm M}_\odot\,({\rm K\,km\,s^{-1}\,pc^2})^{-1}$ for the ^{12}CO(2→1) transition (Leroy et al. 2009; Bolatto et al. 2013). While this Galactic $\alpha_{\rm CO21}$ is allowed within our radiative transfer models, it typically lies in the low-value tail of the resulting distributions, making it less likely. We emphasize that adopting a fixed Galactic conversion factor would not significantly alter our main conclusions. Molecular gas masses and turbulent pressure would decrease by a factor of three, virial ratios would increase by the same factor. Molecular gas fractions would span the range 0.2–0.7, with a median value around 0.35. Our estimates of the total cold gas mass, mass outflow rate and loading factor would be reduced by approximately a factor of two. Therefore, while absolute masses remain sensitive to the choice of $X_{\rm CO}$, our detection statistics, kinematics, virial and pressure analyses, and mass-loading estimates are robust to plausible conversion factor choices. In any case, we would consistently find an observed population of molecular clumps that are gravitationally unbound and exhibit high levels of internal turbulent pressure.

6.5. A tentative interpretation

Finally, in this section we propose a speculative interpretation that synthesizes all the observational evidence gathered so far, and is supported by detailed astrochemical modeling (Noon et al., in prep.). In this picture, illustrated in Figure 8, a hot wind is generated by either the star-formation activity or by supermassive black hole activity in the GC. As the hot wind impacts the surrounding interstellar medium, some cold gas clouds become entrained within it. Initially, these clouds are in chemical equilibrium and consist of molecular gas clumps embedded within an atomic hydrogen envelope (a).

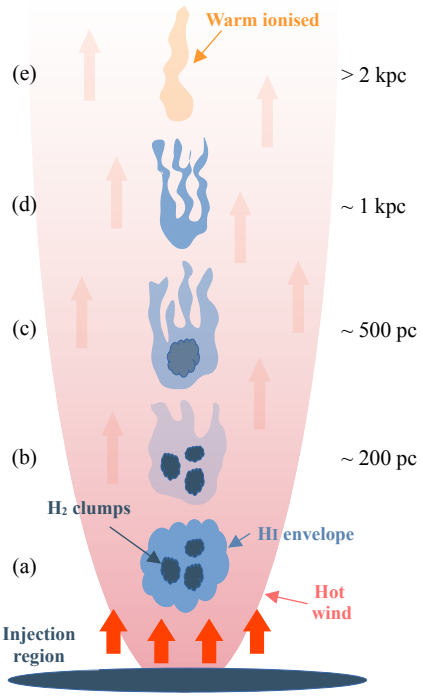

Fig. 8. Cartoon illustrating a possible scenario for the evolution of cold gas clouds in the MW nuclear wind. (a) ISM clouds in chemical equilibrium are entrained in the hot wind; (b) outer HI envelope is depleted and molecular gas exposed; (c) molecular gas dissociates into HI; (d) only HI gas left in the cloud; (e) HI ionizes into HII.

As the clouds flow away, ram pressure by the fast-moving hot gas and turbulent mixing at the cloud interface strip the outer HI layer, which is then ionized by the ambient radiation field and cosmic rays (b). At this stage, the observed clouds exhibit high molecular gas fractions (Sect. 5.5) and appear to be out of chemical equilibrium, showing an overabundance of H_2 relative to HI (Noon et al. 2023). The interaction with the hot wind also increases the level of turbulence (Gerrard et al. 2024), accounting for the observed broad line widths (Sect. 5.3) and large virial parameters (Heyer et al. 2025, and Sect. 5.4). Without the outer HI shielding layer, and under the influence of internal turbulent pressure, the H_2 clumps expand and become exposed to the ambient radiation field, which leads to their rapid dissociation and to the reformation of HI (c). Once the dissociation process is complete, at distances $\gtrsim 1$ kpc, the remaining clouds are dominated by atomic gas (d) with little or no molecular component (Sect. 5.5). At even larger distances, the HI clouds may themselves become ionized or be destroyed by mixing with the surrounding fast-moving hot gas (e) (Lockman et al., in prep.), contributing to the warm ionized gas component detected at higher latitudes with UV absorption studies (Fox et al. 2015; Bordoloi et al. 2017).

7. Summary and conclusions

In this work, we have conducted a systematic search for molecular gas in the nuclear wind of the MW. Using the Atacama Pathfinder EXperiment (APEX), we mapped the ^{12}CO(2→1) emission line toward 19 high–velocity HI clouds that are believed to be entrained in the Galactic center outflow. The data reach a typical sensitivity of 30–80 mK in a 0.5 $\rm km\,s^{-1}$ velocity channel and have a spatial resolution of 28.6″, corresponding to ~1 pc at the distance of the Galactic center.

The main results of our analysis can be summarized as follows:

- High–velocity ^{12}CO(2→1) emission is detected in 12 of the 19 APEX fields. Accounting for secondary high–velocity components that fall within some maps, this yields CO associated with a total of 16 H I wind clouds. No cloud was detected in the ^{12}CO(4→3) transition. We also report non-detections in HCN(2→1) and HCO$^+$(2→1) for MW-C1;
- After segmentation, 207 distinct molecular clumps are identified in the 16 HI clouds with CO detections. Most of HI clouds show a few well-defined molecular clumps. Three clouds have more complex structures, in terms of both their morphology and their kinematics. These clumps represent the coldest phase of the known multiphase outflow;
- The identified CO clumps are compact, with typical radii of $R \sim 1$–3 pc, show relatively large linewidths ($\sigma_v \lesssim 6$ km s^{-1}), and have low CO luminosities ($L_{CO} \sim 0.3$–430 K km s^{-1} pc^2) compared to giant molecular clouds in the MW's disk;
- We constrained the CO–to–H_2 conversion factor in the wind with grids of DESPOTIC radiative–transfer models tailored to the measured W_{CO}, clump radii, HI column densities, and turbulent line widths. The inferred $X_{CO(2-1)}$ values range between $5–20 \times 10^{20}$ cm^{-2} (K km s^{-1})$^{-1}$, several times larger than the canonical Galactic value for the (2→1) transition;
- Wind clumps lie on the classical mass–radius relation for disk molecular clouds, extending it to the low-mass end. Conversely, in the linewidth-radius and linewidth-mass planes, they show systematically larger dispersions than disk clouds, indicating an excess of turbulent motions. A virial analysis shows that most clumps have $M_{vir} \gg M_{mol}$, with α_{vir} ranging from a few to several hundred, implying that the vast majority (~90%) are gravitationally unbound;
- High velocity dispersions suggest a high level of turbulence, which might be driven by the cloud-wind interaction at the cloud interface; for example, through shear instabilities. Turbulence leads to large internal (turbulent) pressures, $P_{int}/k \sim 10^4$–10^7 K cm^3. External confinement by ambient pressure can help some clumps survive, but matching the internal pressures of the full sample would require hot–phase conditions ($n \sim 10^{-1}$ cm^{-3}, $T \sim 10^7$ K) out to ~1 kpc that are unlikely given theoretical expectations and X–ray constraints. A good fraction of clumps is probably expanding, which may lead to the eventual disruption of molecules;
- For clouds with CO detections, we measure high molecular mass fractions, typically $f_{mol} \simeq 0.6$–0.9, with only two cases near $f_{mol} \simeq 0.3$. We find no clear trend of f_{mol} with height over $z \lesssim 1$ kpc, nor a correlation with peak HI column density. Interestingly, we detect no CO at latitudes $|b| \gtrsim 7°$ (projected $z \sim 1$ kpc), indicating that molecular gas is rapidly dissociated beyond this height, with typical timescales of $\lesssim$3 Myr. The rapid decline suggests that molecular gas is short–lived in the wind, favoring an entrainment–plus–dissociation scenario rather than in situ molecule formation at high height.

In conclusion, our study significantly expands the known molecular component of the Galactic center wind, providing the first statistical characterization of molecular clouds in the outflow. Our observations demonstrate that the Galactic center wind hosts a populous, molecule–rich clump population below ~1 kpc that is kinematically hot, largely unbound, and likely shaped by the interaction with the surrounding hot flow. These results highlight that the MW's nuclear wind is a powerful laboratory for studying cold–hot coupling in multiphase outflows, providing quantitative benchmarks for high-resolution simulations of cloud survival, confinement, and dissociation in galactic winds.

Acknowledgements. The authors warmly thank the technicians and the scientists who carried out the observations at the APEX telescope. This work was performed in part at the Aspen Center for Physics, which is supported by National Science Foundation (NSF) grant PHY-2210452, and in part at the Research School of Astronomy and Astrophysics, the Australian National University. EDT, AF, NP and QY were supported by the European Research Council (ERC) under grant agreement no. 101040751. MRK and NM-G acknowledge support from the Australian Research Council through Laureate Fellowships FL220100020 and FL210100039, respectively. LA acknowledges support through the Program "Rita Levi Montalcini" of the Italian MIUR. MPB acknowledges support from the National Radio Astronomy Observatory through the Jansky Fellowship. This publication is based on data acquired with the Atacama Pathfinder Experiment (APEX), under project codes 0104.B-0106A, 0106.B-0034A and 0106.C-0031A. APEX is a collaboration between the Max-Planck-Institut fur Radioastronomie, the European Southern Observatory, and the Onsala Space Observatory. The GBT data were obtained under project codes 21A_240 and 22A_339. The Green Bank Telescope is a facility of the National Science Foundation and part of the National Radio Astronomy Observatory. It is operated by Associated universities, Inc., under a cooperative agreement with the NSF.

References

Armillotta, L., Fraternali, F., Werk, J. K., Prochaska, J. X., & Marinacci, F. 2017, MNRAS, 470, 114
Armillotta, L., Krumholz, M. R., & Di Teodoro, E. M. 2020, MNRAS, 493, 5273
Armillotta, L., Ostriker, E. C., Kim, C.-G., & Jiang, Y.-F. 2024, ApJ, 964, 99
Banda-Barragán, W. E., Brüggen, M., Heesen, V., et al. 2021, MNRAS, 506, 5658
Barnes, A. T., Longmore, S. N., Battersby, C., et al. 2017, MNRAS, 469, 2263
Bertoldi, F., & McKee, C. F. 1992, ApJ, 395, 140
Bland-Hawthorn, J., Maloney, P. R., Sutherland, R., et al. 2019, ApJ, 886, 45
Bolatto, A. D., Wolfire, M., & Leroy, A. K. 2013, ARA&A, 51, 207
Bordoloi, R., Fox, A. J., Lockman, F. J., et al. 2017, ApJ, 834, 191
Bordoloi, R., Fox, A. J., & Lockman, F. J. 2025, ApJ, 987, L32
Brüggen, M., & Scannapieco, E. 2016, ApJ, 822, 31
Burton, W. B., & Liszt, H. S. 1978, ApJ, 225, 815
Bustard, C., Zweibel, E. G., & D'Onghia, E. 2016, ApJ, 819, 29
Cashman, F. H., Fox, A. J., Savage, B. D., et al. 2021, ApJ, 923, L11
Cashman, F. H., Fox, A. J., Wakker, B. P., et al. 2023, ApJ, 944, 65
Chen, B. Q., Li, G. X., Yuan, H. B., et al. 2020, MNRAS, 493, 351
Chevalier, R. A., & Clegg, A. W. 1985, Natur, 317, 44
Crocker, R. M., Bicknell, G. V., Taylor, A. M., & Carretti, E. 2015, ApJ, 808, 107
Deng, Y., Li, Z., Li, Z., et al. 2025, MNRAS, 538, 2445
Di Teodoro, E. M., & Fraternali, F. 2015, MNRAS, 451, 3021
Di Teodoro, E. M., McClure-Griffiths, N. M., Lockman, F. J., et al. 2018, ApJ, 855, 33
Di Teodoro, E. M., McClure-Griffiths, N. M., Lockman, F. J., & Armillotta, L. 2020, Natur, 584, 364
Draine, B. T. 1978, ApJS, 36, 595
Federrath, C., Roman-Duval, J., Klessen, R. S., Schmidt, W., & Mac Low, M. M. 2010, A&A, 512, A81
Fielding, D. B., & Bryan, G. L. 2022, ApJ, 924, 82
Fluetsch, A., Maiolino, R., Carniani, S., et al. 2019, MNRAS, 483, 4586
Fox, A. J., Bordoloi, R., Savage, B. D., et al. 2015, ApJ, 799, L7
Gerrard, I. A., Noon, K. A., Federrath, C., et al. 2024, MNRAS, 530, 4317
Gildas Team. 2013, GILDAS: Grenoble Image and Line Data Analysis Software, Astrophysics Source Code Library
Ginsburg, A., Henkel, C., Ao, Y., et al. 2016, A&A, 586, A50
Gong, M., Ostriker, E. C., & Wolfire, M. G. 2017, ApJ, 843, 38
GRAVITY Collaboration (Abuter, R., et al.) 2019, A&A, 625, L10
Gronke, M., & Oh, S. P. 2020, MNRAS, 492, 1970
Grønnow, A., Tepper-García, T., Bland-Hawthorn, J., & Fraternali, F. 2022, MNRAS, 509, 5756
Hennebelle, P., & Falgarone, E. 2012, A&A Rev., 20, 55
Henshaw, J. D., Barnes, A. T., Battersby, C., et al. 2023, in Astronomical Society of the Pacific Conference Series, 534, Protostars and Planets VII, eds. S. Inutsuka, Y. Aikawa, T. Muto, K. Tomida, & M. Tamura, 83
Heyer, M., & Dame, T. M. 2015, ARA&A, 53, 583
Heyer, M., Di Teodoro, E., Loinard, L., et al. 2025, A&A, 695, A60
Kanjilal, V., Dutta, A., & Sharma, P. 2021, MNRAS, 501, 1143

Kim, C.-G., Ostriker, E. C., Somerville, R. S., et al. 2020, ApJ, 900, 61
Krumholz, M. R. 2014, MNRAS, 437, 1662
Krumholz, M. R., Crocker, R. M., & Offner, S. S. R. 2023, MNRAS, 520, 5126
Larson, R. B. 1981, MNRAS, 194, 809
Lelli, F., Verheijen, M., & Fraternali, F. 2014, MNRAS, 445, 1694
Leroy, A. K., Walter, F., Bigiel, F., et al. 2009, AJ, 137, 4670
Leroy, A. K., Hughes, A., Liu, D., et al. 2021, ApJS, 255, 19
Lewis, J. A., Lada, C. J., & Dame, T. M. 2022, ApJ, 931, 9
Lockman, F. J. 1984, ApJ, 283, 90
Lockman, F. J., & McClure-Griffiths, N. M. 2016, ApJ, 826, 215
Lockman, F. J., Di Teodoro, E. M., & McClure-Griffiths, N. M. 2020, ApJ, 888, 51
McClure-Griffiths, N. M., Pisano, D. J., Calabretta, M. R., et al. 2009, ApJS, 181, 398
McClure-Griffiths, N. M., Green, J. A., Hill, A. S., et al. 2013, ApJ, 770, L4
Miller, M. J., & Bregman, J. N. 2016, ApJ, 829, 9
Miville-Deschênes, M.-A., Murray, N., & Lee, E. J. 2017, ApJ, 834, 57
Naab, T., & Ostriker, J. P. 2017, ARA&A, 55, 59
Nagata, M., Egusa, F., Maeda, F., et al. 2025, ApJ, 987, 69
Neubert, P., & Protzel, P. 2014, in 22nd International Conference on Pattern Recognition (IEEE), 996
Nogueras-Lara, F., Schödel, R., Gallego-Calvente, A. T., et al. 2020, Nat. Astron., 4, 377
Noon, K. A., Krumholz, M. R., Di Teodoro, E. M., et al. 2023, MNRAS, 524, 1258
Oka, T., Geballe, T. R., Goto, M., et al. 2019, ApJ, 883, 54
Padovani, M., Ivlev, A. V., Galli, D., et al. 2020, SSRv, 216, 29
Peschken, N., Hanasz, M., Naab, T., Wóltański, D., & Gawryszczak, A. 2023, MNRAS, 522, 5529
Ponti, G., Hofmann, F., Churazov, E., et al. 2019, Natur, 567, 347
Ponti, G., Morris, M. R., Churazov, E., Heywood, I., & Fender, R. P. 2021, A&A, 646, A66
Predehl, P., Sunyaev, R. A., Becker, W., et al. 2020, Nature, 588, 227
Rathjen, T.-E., Naab, T., Walch, S., et al. 2023, MNRAS, 522, 1843
Richings, A. J., & Faucher-Giguère, C.-A. 2018, MNRAS, 478, 3100
Roberts, M. S. 1975, Radio Observations of Neutral Hydrogen in Galaxies, eds. A. Sandage, M. Sandage, & J. Kristian (the University of Chicago Press), 309
Roman-Duval, J., Jackson, J. M., Heyer, M., Rathborne, J., & Simon, R. 2010, ApJ, 723, 492
Rosolowsky, E., & Leroy, A. 2006, PASP, 118, 590
Rosolowsky, E. W., Pineda, J. E., Kauffmann, J., & Goodman, A. A. 2008, ApJ, 679, 1338
Rosolowsky, E., Hughes, A., Leroy, A. K., et al. 2021, MNRAS, 502, 1218
Sarkar, K. C. 2024, A&A Rev., 32, 1
Sarkar, K. C., Nath, B. B., & Sharma, P. 2015, MNRAS, 453, 3827
Scannapieco, E., & Brüggen, M. 2015, ApJ, 805, 158
Schneider, E. E., & Robertson, B. E. 2017, ApJ, 834, 144
Schneider, E. E., Ostriker, E. C., Robertson, B. E., & Thompson, T. A. 2020, ApJ, 895, 43
Schödel, R., Feldmeier, A., Kunneriath, D., et al. 2014, A&A, 566, A47
Solomon, P. M., Rivolo, A. R., Barrett, J., & Yahil, A. 1987, ApJ, 319, 730
Sormani, M. C., Treß, R. G., Ridley, M., et al. 2018, MNRAS, 475, 2383
Sparre, M., Pfrommer, C., & Ehlert, K. 2020, MNRAS, 499, 4261
Su, M., Slatyer, T. R., & Finkbeiner, D. P. 2010, ApJ, 724, 1044
Su, Y., Zhang, S., Yang, J., et al. 2022, ApJ, 930, 112
Thompson, T. A., & Heckman, T. M. 2024, ARA&A, 62, 529
Thompson, T. A., Fabian, A. C., Quataert, E., & Murray, N. 2015, MNRAS, 449, 147
Thompson, T. A., Quataert, E., Zhang, D., & Weinberg, D. H. 2016, MNRAS, 455, 1830
Veena, V. S., Riquelme, D., Kim, W. J., et al. 2023, A&A, 674, L15
Veilleux, S., Maiolino, R., Bolatto, A. D., & Aalto, S. 2020, A&ARv, 28, 2
Verheijen, M. A. W., & Sancisi, R. 2001, A&A, 370, 765
Vijayan, A., & Krumholz, M. R. 2024, MNRAS, 532, 4132
Vijayan, A., Krumholz, M. R., & Wibking, B. D. 2024, MNRAS, 527, 10095
Vijayan, A., Krumholz, M. R., & Wibking, B. D. 2025, MNRAS, 539, 1706
Wibking, B. D., & Krumholz, M. R. 2023, MNRAS, 521, 5972
Yeung, M. C. H., Ponti, G., Freyberg, M. J., et al. 2024, A&A, 690, A399
Zhang, D., Davis, S. W., Jiang, Y.-F., & Stone, J. M. 2018, ApJ, 854, 110
Zubovas, K., & Nayakshin, S. 2012, MNRAS, 424, 666

Appendix A: Moment maps for detected CO clouds

In this appendix, we show HI and ^{12}CO(2→1) maps for the 16 clouds with detected molecular gas (Figures B.1-B.4). HI maps were derived from GBT data at 540″ resolution (Di Teodoro et al. 2018), while CO maps were derived from APEX data at 28″ resolution. Each row of panels indicates one HI cloud. Clouds labeled with a _2 represent a secondary velocity component detected in the CO APEX data in the same field of the main target.

From left to right, we plot the HI column density map (blue color-scale), the CO integrated intensity map (0th moment, orange color-scale) and the CO LSR velocity map (1st moment, spectral color-scale). The red square in all maps highlights the field observed in CO with APEX. The beam sizes of the GBT and APEX are indicated as gray circles in the HI and CO total maps, respectively. Contour levels on the HI and CO maps are at $2^n \times 2.5\sigma_{\rm rms}$ with $n = 0, 1, 2, 3, 4$, where $\sigma_{\rm rms}$ is the rms noise of the masked 0th moment map (see appendixes of Verheijen & Sancisi 2001; Lelli et al. 2014).

Appendix B: Table of positions and derived masses

Table B.1 lists some global properties of the high-velocity clouds in the MW's nuclear wind followed up in molecular tracers to date. The table includes the 19 clouds observed with APEX and presented here and in Di Teodoro et al. (2020) (clouds 1–19) plus the two clouds observed with LMT (clouds 20 and 21 Heyer et al. 2025) and reanalyzed for this work.

All quantities were derived assuming a fixed distance of 8.2 kpc from the GC. Columns as follow:

1. Cloud assigned name.
2. Galactic longitude, ℓ, in degrees.
3. Galactic latitude, b, in degrees.
4. Central local standard-of-rest velocity, $V_{\rm LSR}$, in $\rm km\,s^{-1}$.
5. Height, z, above (positive) or below (negative) the Galactic plane, in kiloparsecs.
6. Projected distance, d, from the Galactic center, in kiloparsecs.
7. Mass of atomic gas, $M_{\rm at}$, including helium, derived from the GBT HI data, in $\rm M_\odot$.
8. Adopted molecular gas conversion factors, $\alpha_{\rm CO}$ (see Section 4), in $\rm M_\odot\,(K\,km\,s^{-1}\,pc^2)^{-1}$. For non-detections, we used the median value across the sample, $\tilde{\alpha}_{\rm CO} = 22$ $\rm M_\odot\,(K\,km\,s^{-1}\,pc^2)^{-1}$, to estimate upper limits on the molecular mass.
9. Mass of molecular gas, $M_{\rm mol}$, including helium, derived from the ^{12}CO(2→1) APEX data or from the ^{12}CO(1→0) LMT data, in $\rm M_\odot$. For non-detections, we indicate our upper limits based on the rms noise of the data (see Section 3.4).
10. Molecular gas fraction, $f_{\rm mol} = M_{\rm mol}/(M_{\rm at} + M_{\rm mol})$. For non-detections, we indicate upper limits.

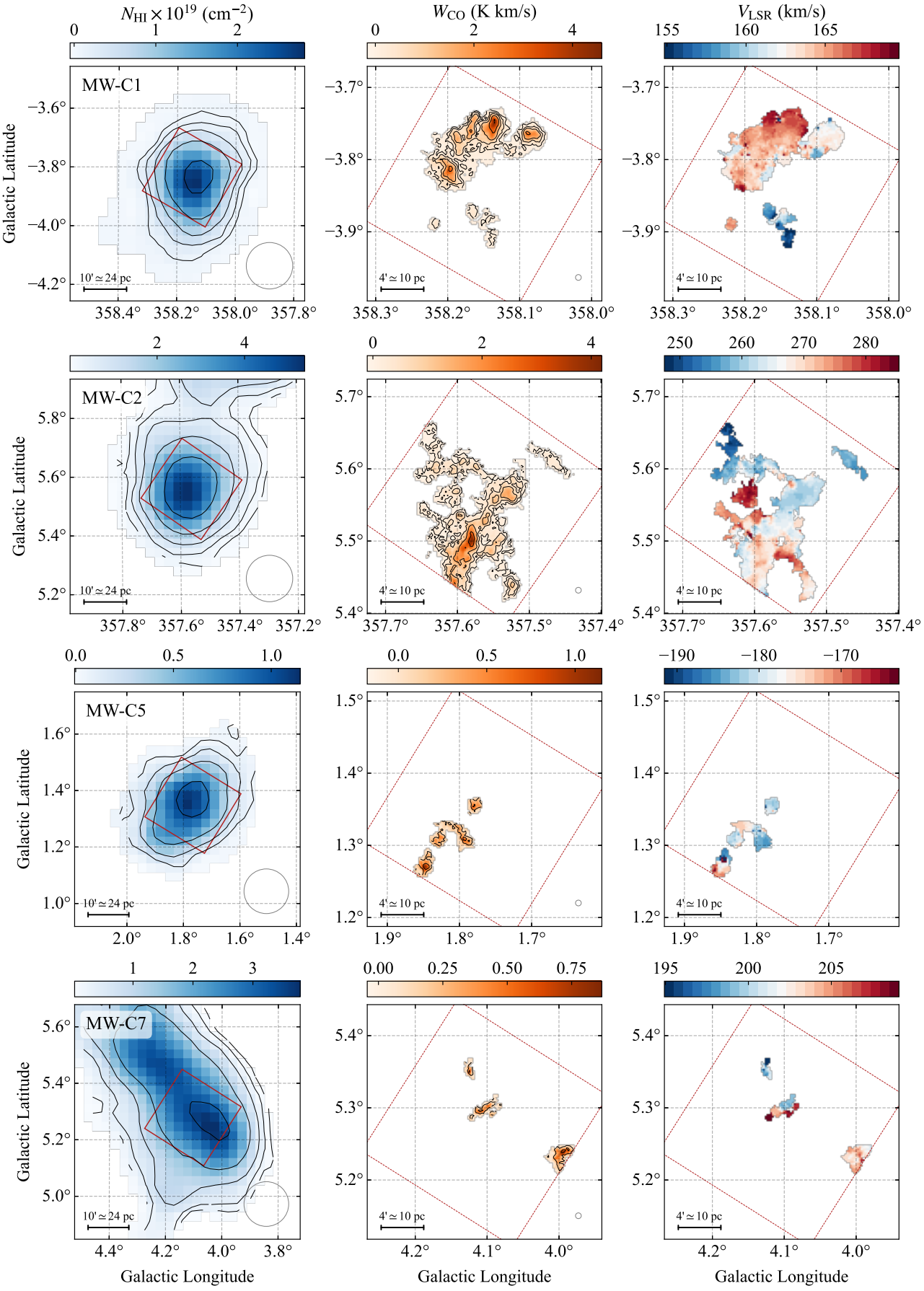

Fig. B.1. Maps of clouds MW-C1, MW-C2, MW-C5 and MW-C7. See Appendix A for details.

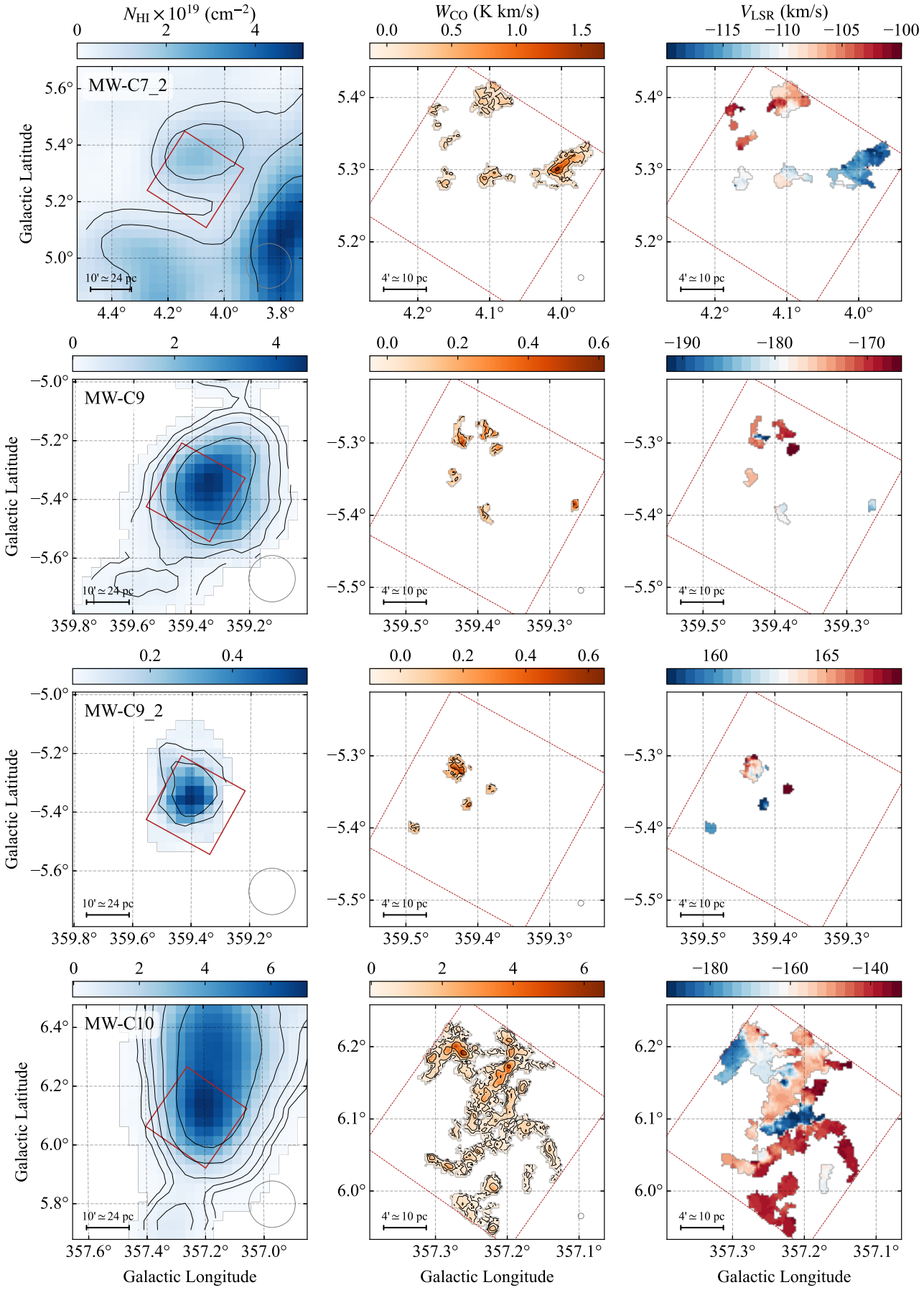

Fig. B.2. Maps of clouds MW-C7_2, MW-C9, MW-C9_2 and MW-C10. See Appendix A for details.

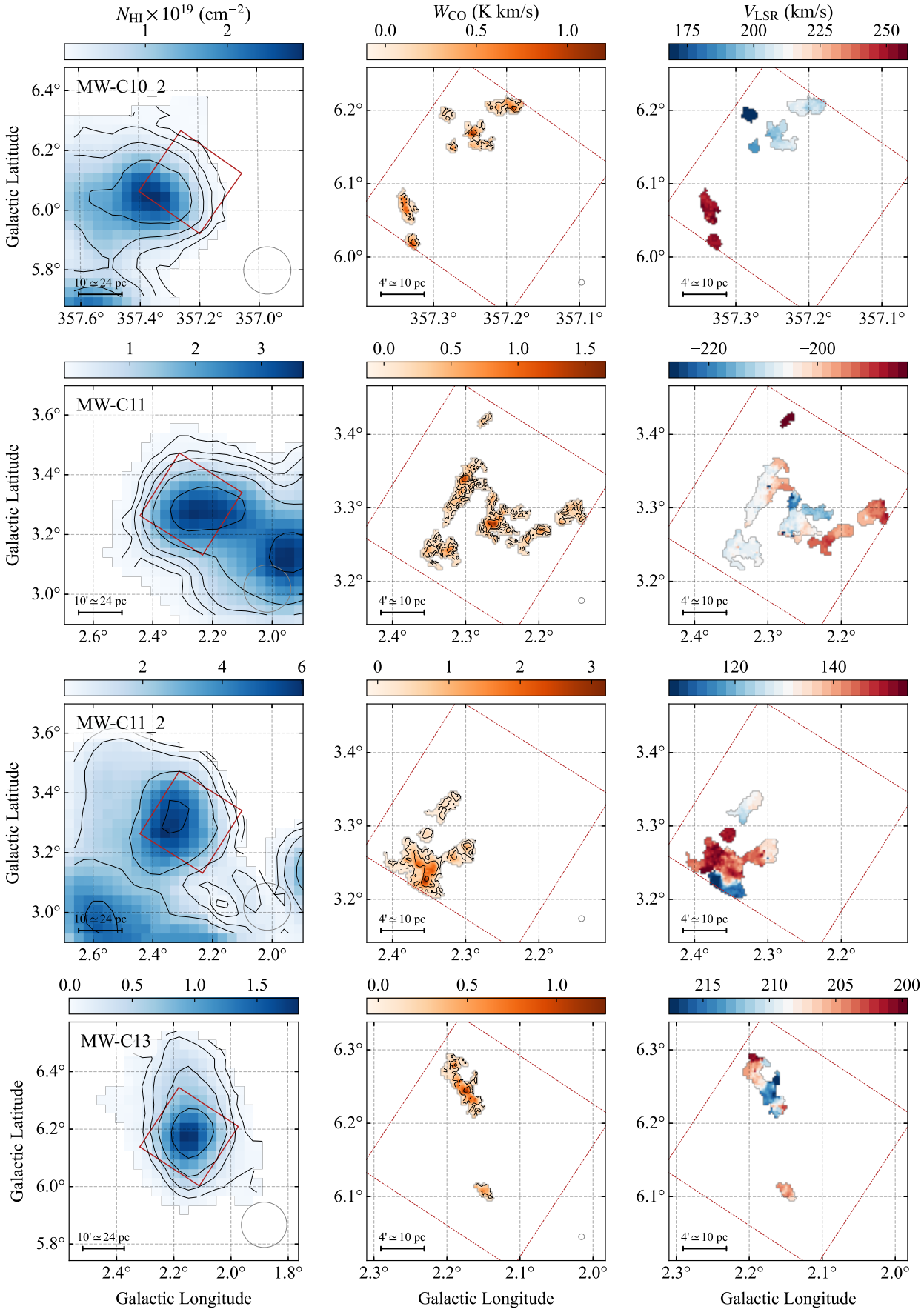

Fig. B.3. Maps of clouds MW-C10_2, MW-C11, MW-C11_2 and MW-C13. See Appendix A for details.

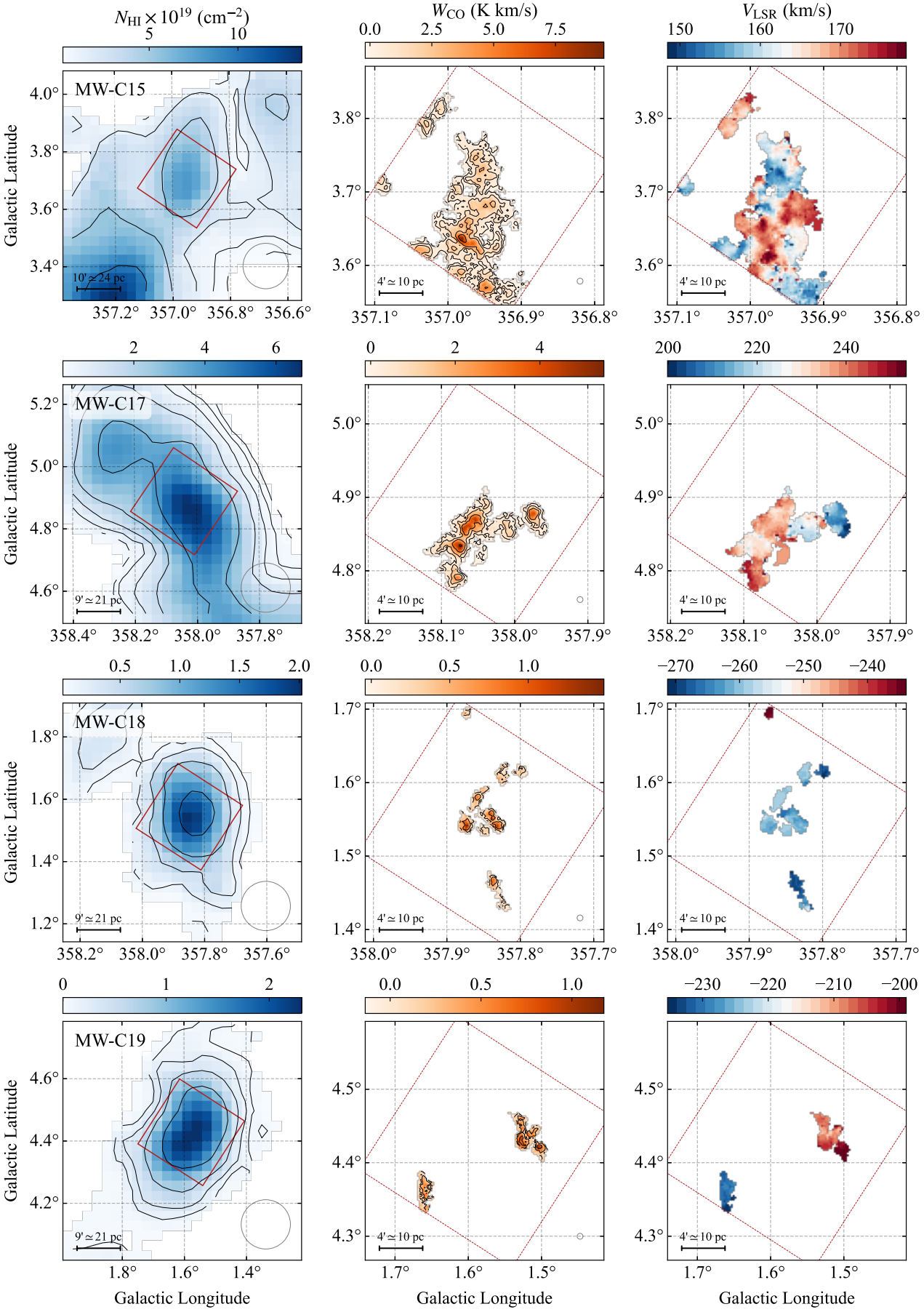

Fig. B.4. Maps of clouds MW-C15, MW-C17, MW-C18 and MW-C19. See Appendix A for details.

Table B.1. Derived masses of the cloud sample.

Name	ℓ (°)	b (°)	$V_{\rm LSR}$ (km s^{-1})	z (kpc)	d (kpc)	$M_{\rm at}$ ($M_\odot$)	$\alpha_{\rm CO}$	$M_{\rm mol}$ ($M_\odot$)	$f_{\rm mol}$
MW-C1	−1.85	−3.83	+163	−0.55	0.61	250	23^{+39}_{-13}	3022^{+2369}_{-801}	$0.93^{+0.02}_{-0.04}$
MW-C2	−2.44	+5.56	+265	+0.80	0.87	585	21^{+45}_{-14}	3792^{+2692}_{-816}	$0.87^{+0.03}_{-0.06}$
MW-C3†	+13.30	+7.13	−100	+1.02	2.16	944	–	< 30	< 0.03
MW-C4†	+1.66	+5.11	−262	+0.73	0.77	105	–	< 38	< 0.27
MW-C5	+1.77	+1.35	−178	+0.19	0.32	110	33^{+35}_{-15}	384^{+178}_{-70}	$0.78^{+0.04}_{-0.06}$
MW-C6†	+8.82	+9.67	+200	+1.38	1.87	101	–	< 20	< 0.17
MW-C7	+4.10	+5.28	+205	+0.76	0.96	560	28^{+40}_{-15}	231^{+205}_{-74}	$0.30^{+0.09}_{-0.10}$
MW-C7_2	+4.14	+5.36	−110	+0.76	0.96	265	31^{+37}_{-15}	852^{+570}_{-230}	$0.77^{+0.06}_{-0.10}$
MW-C8†	+3.50	+8.62	+365	+1.24	1.33	132	–	< 24	< 0.16
MW-C9	−0.61	−5.37	−175	−0.77	0.77	532	36^{+46}_{-16}	238^{+126}_{-45}	$0.31^{+0.06}_{-0.07}$
MW-C9_2	−0.56	−5.30	+163	−0.77	0.77	30	52^{+73}_{-24}	242^{+251}_{-83}	$0.89^{+0.04}_{-0.07}$
MW-C10	−2.77	+6.10	−165	+0.87	0.96	884	20^{+48}_{-14}	6105^{+3217}_{-943}	$0.87^{+0.03}_{-0.04}$
MW-C10_2	−2.67	+6.04	+210	+0.87	0.96	157	33^{+41}_{-15}	540^{+266}_{-99}	$0.78^{+0.04}_{-0.07}$
MW-C11	+2.24	+3.28	−203	+0.47	0.57	441	42^{+66}_{-24}	1543^{+957}_{-350}	$0.78^{+0.05}_{-0.08}$
MW-C11_2	+2.33	+3.33	+130	+0.47	0.57	644	17^{+28}_{-10}	1042^{+614}_{-211}	$0.62^{+0.07}_{-0.10}$
MW-C12†	−4.75	+8.69	−188	+1.24	1.42	151	–	< 26	< 0.15
MW-C13	+2.15	+6.18	−217	+0.88	0.94	158	23^{+33}_{-12}	345^{+264}_{-98}	$0.69^{+0.07}_{-0.12}$
MW-C14†	+13.01	−7.64	−182	−1.09	2.15	170	–	< 22	< 0.12
MW-C15	−3.05	+3.71	+168	+0.53	0.69	1015	12^{+24}_{-7}	4595^{+2203}_{-703}	$0.82^{+0.03}_{-0.05}$
MW-C16†	−1.99	+12.53	−136	+1.79	1.82	771	–	< 32	< 0.04
MW-C17	−1.96	+4.89	+230	+0.70	0.75	918	12^{+23}_{-7}	1706^{+1249}_{-411}	$0.66^{+0.08}_{-0.11}$
MW-C18	−2.15	+1.55	−258	+0.22	0.38	197	37^{+61}_{-20}	769^{+477}_{-160}	$0.80^{+0.05}_{-0.07}$
MW-C19	+1.58	+4.43	−226	+0.63	0.67	255	43^{+65}_{-22}	553^{+437}_{-149}	$0.69^{+0.07}_{-0.11}$
MW-C20⋆†	+1.55	+3.74	−235	0.53	0.58	284	–	< 22	< 0.07
MW-C21⋆	−1.14	+3.73	+165	0.54	0.56	462	9^{+16}_{-5}	215^{+216}_{-70}	$0.33^{+0.10}_{-0.11}$

† Non-detection.
⋆ ^{12}CO(1→0) data from Heyer et al. (2025).

Notes. See Appendix B for details on the columns.